Diploma Thesis

Integrating Transparent Conductors and Optics in Microfabricated Ion Traps to Enable Next-Generation Quantum Computing

submitted in satisfaction of the requirements for the degree
Diplom-Ingenieur
of the TU Wien, Faculty of Applied Physics

Diplomarbeit

Integration von transparenten Leitern und Optik in mikrofabrizierten Ionenfallen

ausgeführt zum Zwecke der Erlangung des akademischen Grads
Diplom-Ingenieur
eingereicht an der TU Wien, Fakultät für Technische Physik

Matthias Preidl, BSc

Matr.Nr.: 11701284

Betreuung: Univ.Prof.in Dipl.-Ing. Dr.in techn. Dr.in h.c. **Ulrike Diebold**[1]
Univ.Ass.in Mag.a rer.nat. Dr.in rer.nat. **Margareta Wagner**[1]
Dr. **Klemens Schüppert**[2]
Dr. **Clemens Rössler**[2]
[1]Institut für Angewandte Physik
Forschungsbereich Oberflächenphysik
Technische Universität Wien
Wiedner Hauptstr. 8-10/134, 1040 Wien, Österreich
[2]Infineon Technologies Austria AG
Siemensstraße 2, 9500 Villach, Österreich

Wien, im August 2023 _____

Chapter 1

Abstract

Integrating photonics into ion traps remains an inevitable hurdle that needs to be overcome in order to allow scaling of trapped ion quantum computers. This thesis aims to enhance trapped ion quantum computing by tackling the challenges posed by the integration of dielectrics into the next generation of trapped ion quantum computers in the form of optical components. Dielectrics have been found to adversely affect ion stability, resulting in reduced fidelity and coherence times. To mitigate these effects, this study explores novel materials like transparent conducting oxides such as Al:ZnO and innovative combinations of existing materials in the form of dielectric (Al_2O_3)-metal (Au) stacks. An array of analytical techniques is employed to evaluate the effectiveness and composition of these materials. Beyond typical transmission and sheet resistance measurements, we delve deeper into the effects of annealing and cryogenic temperatures on sheet resistance which become relevant in the fabrication and operation steps of ion traps. Moreover, comprehensive evaluations are conducted, utilising AFM, SEM, TEM and KPFM, to investigate film quality and growth characteristics. The findings show that Al:ZnO and Al_2O_3-gold films demonstrate the highest potential as shielding layers, effectively safeguarding trapped ions from disruptive dielectric charges while preserving optical access.

Die Integration von Photonik in Ionenfallen stellt nach wie vor eine unvermeidliche Hürde dar, die überwunden werden muss, um die Skalierung von Ionen-basierten Quantencomputern zu ermöglichen. Das Ziel dieser Arbeit besteht darin, Ionenfallen zu verbessern, indem die Probleme gelöst werden, die sich aus der Integration von Dielektrika in Form von photonischen Bauteilen entstehen. Es wurde experimentell sowie theoretisch festgestellt, dass Dielektrika die Ionenstabilität beeinträchtigen. Um die hervorgerufenen Effekte zu verhindern, werden in dieser Arbeit neuartige Materialien wie transparente leitfähige Oxide wie Al:ZnO sowie neue Kombinationen bestehender Materialien in Form von dielektrischen (Al_2O_3)-Metall (Au)-Stacks untersucht. Zur Beurteilung der Effiktivität und Zusammensetzung dieser Materialien werden verschiedene analytische Techniken angewendet. Neben den herkömmlichen Transmissions- und Schichtwiderstandsmessungen werden auch die Auswirkungen von Hoch- und Tieftemperaturen auf den Schichtwiderstand untersucht, da diese für die Herstellung und den Betrieb von Ionenfallen von Bedeutung sind. Darüber hinaus erfolgen umfassende Auswertungen mittels AFM, SEM, TEM und KPFM, um die Schichtqualität und Wachstumseigenschaften zu untersuchen.Die Ergebnisse zeigen, dass Al:ZnO und Al_2O_3-Gold Filme das größte Potenzial als Abschirmungsschichten aufweisen um die eingefangene Ionen effektiv vor störenden dielektrischen Ladungen zu schützen und gleichzeitig den optischen Zugang bewahren.

Contents

Chapter 2

Introduction

The potential of atoms has long been harnessed for destructive purposes in nuclear reactions, but their untapped quantum mechanical behaviour offers an even more compelling prospect - quantum computing. The idea of utilising charged particles to execute logical operations traces back to the advent of semiconductors and the development of logical gates in silicon. Over time, numerous iterations have emerged, aimed at optimising energy efficiency and size, ranging from large power MOSFETs to nanometre-scale FinFETs. To foster the widespread adoption of this technology, entire industries have emerged, solely focused on refining the construction of integrated circuit products and enhancing their performance parameters. Innovations have even led to the implementation of new materials like III-V semiconductors, such as GaN, further augmenting semiconductor functionality. Despite their pervasive usage and undeniable impact on revolutionising human experiences, conventional semiconductor technologies are approaching their limits when it comes to tackling next-level challenges.

One of the foremost and widely recognised constraints afflicting modern chips pertains to the deceleration of Moore's law - the exponential reduction in structural size. The minute dimensions, reaching down to a few nanometres, have now approached the physical limits of feasible construction and control. Consequently, these devices, governed by classical physics, are gradually yielding to quantum mechanical effects, rendering their intended functionality unviable. The implications extend to the increasingly arduous task of enhancing computing power.

A crucial design drawback in contemporary semiconductor chips lies in their inherent binary nature, wherein they can only represent information as either 1 or 0. Consequently, tackling intricate problems becomes exponentially more challenging. For instance, numerous simulation challenges encountered in natural systems, such as molecular simulations, can only be approximated by today's computers. To gain profound insights into such systems, the underlying computing architecture must embrace a quantum mechanical framework. Additionally, problems involving numerous variables, such as mazes, prime factorisation, and the traveling salesman problem, which are classified as NP complete problems, necessitate either novel algorithms or advanced technologies for efficient resolution [1].

Enabling new frontiers in computing demands harnessing the quantum mechanical properties of particles. Despite numerous conceptualisations and developments in quantum computing designs, only a select few have managed to attain a feasible status, out of which superconducting qubits and trapped ion qubits have emerged as the most viable options, embraced by leading computing industry [2]. In this thesis, the primary focus will centre on the utilisation of trapped ion quantum computers, specifically shedding light on novel materials and procedures for eliminating dielectric noise sources.

Chapter 3

Fundamentals

3.1 Capturing an ion

Achieving the capture and isolation of a particle in order to preserve its quantum coherence poses a formidable challenge. For instance, effectively isolating a solitary gaseous atom demands cooling it to temperatures as low as millikelvin while constraining it with powerful and precise laser beams [3]. In contrast, when dealing with single ions, as the name suggests, they can be confined through the utilisation of electric fields rather than light. However, contrary to their seemingly simpler nature compared to neutral counterparts, trapping ions reveal inherent complexities. The trapping process requires alternating current radio frequencies, as it is physically impossible to trap an ion using a DC electric field [4].

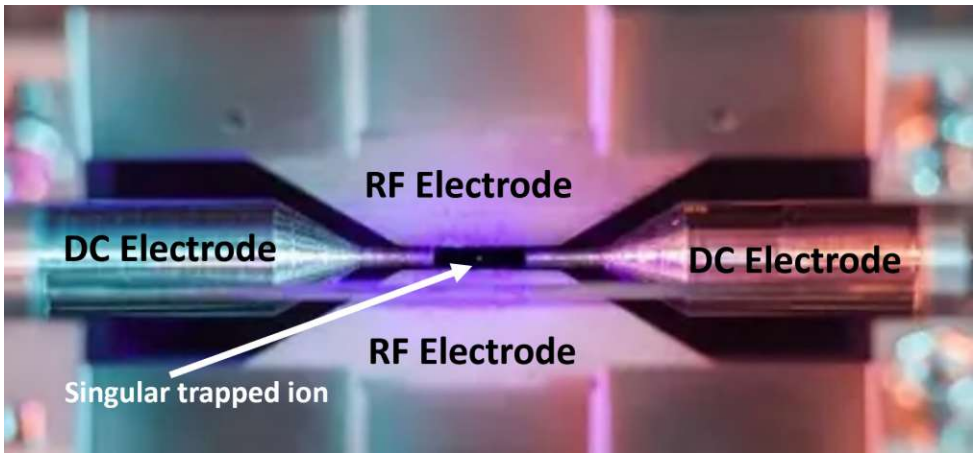

Fig. 3.1: An image of a single ion trapped in a UHV setup using a macroscopic Paul trap, the fluorescence of the ion is made visible using a long exposure setting on a camera and is caused by external lasers [5].

The process of loading an ion into the trap entails sublimating atoms from an oven, followed by laser-induced isotope specific photoionisation. However, capturing an ion in the potential well and preserving its position pose additional challenges. It becomes necessary to avoid any interaction between the trapped ions and the surrounding environment, such as gas particles. To mitigate the risks of collisions with gas molecules, the ion trapping setup is constructed within an ultra-high vacuum (UHV) chamber, pumped down to 10^{-10} mbar or lower. Moreover, to further curtail gas-ion interactions, the chamber is maintained at cryogenic temperatures. Beyond isolating the ion from impinging particles, its coherence may also be jeopardised by stray electric and magnetic fields. Therefore, within the vacuum chamber, the trapping apparatus is commonly shielded within a Faraday cage, typically milled from high-purity copper, or alternatively, μ-metal shields can be employed for enhanced protection. Through these and other techniques, the trapped ion

is significantly isolated from external disturbances, minimising potential sources of interference [6]. Figure 3.1 displays a photograph of an ion successfully trapped using the equipment and processes described.

3.2 Laser addressing of ions

3.2.1 Laser cooling

The effective control and precise addressing of trapped ions, both in their electronic and motional states, relies on coherent electromagnetic radiation fine-tuned to match their transition energies. In this thesis, the focus predominantly centres on employing laser light to achieve the desired transitions for ions. However, microwaves could also facilitate these transitions [7]. Regardless of the chosen method for inducing qubit states or transitions, whether through magnetic fields, microwaves, or lasers, reliable ion operations necessitates cooling the ion close to its ground state. Techniques such as doppler cooling and sideband cooling are used to achieve the desired cooling effect and their use is displayed in figure 3.2 below. Both mechanisms utilise lasers as a means to induce the cooling process [8].

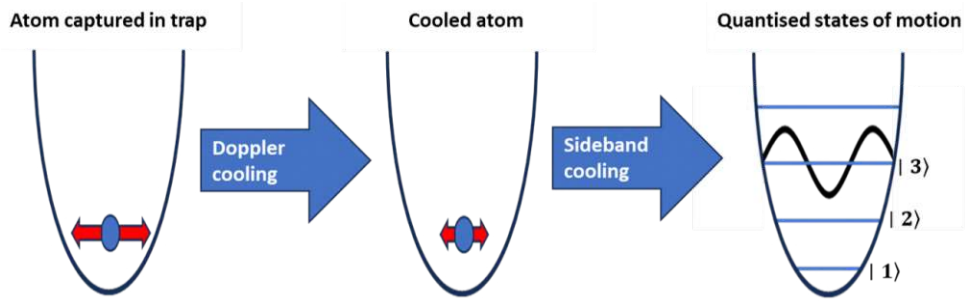

Fig. 3.2: Once an ion is trapped in a potential well it still has considerable axial motional modes that need to be reduced. In a cooled atom the magnitude of these oscillations is considerably reduced, as is indicated by the smaller red arrows. In theory an ion can be cooled down so far that the states of motion become quantised

3.2.2 Doppler cooling

The initial cooling steps involve the application of doppler cooling, a mechanism harnessing the phenomenon of random directionality of photoemission processes. The impulse on the ion resulting from an emitted photon is inherently random. Consequently, during cycles of photon absorption and emission, the ion fails to cool down adequately, given the imparting of impulses in all directions indiscriminately. However, this limitation can be overcome by slightly red detuning the photoemission inducing laser, ensuring that the ion becomes excited only when moving towards the laser. Through averaging the random emissions and enabling directionally controlled excitation over numerous cycles, the ion's kinetic energy is gradually reduced, facilitating cooling. This however is only possible down to a certain ion temperature, the doppler limit. To achieve ground-state cooling other mechanisms need to be implemented [9].

3.2.3 Sideband cooling

Sideband cooling is a technique which can be employed to achieve near-ground state cooling of the ion, reducing its motional energy to the point of possessing zero-point energy. This cooling

method capitalises on the quantisation of both the ion's motional and internal electronic states. The process involves utilising a red-detuned laser to induce excitation from a motional sideband to a higher electronic spin state while maintaining the same motional state reduced by one quanta of motion. Left to naturally decay from this state, the ion would undergo cooling via relaxation back into the original electronic state. Due to the stability of the excited state this natural decay takes too long for efficient cooling. However, by exciting the ion using a dipole laser, it allows for decay via the fast blue transition back into the electronic ground state. By repeating this sequence multiple times see figure 3.3, the ion can be progressively cooled close to its ground state, achieving the desired near-zero motional energy [10].

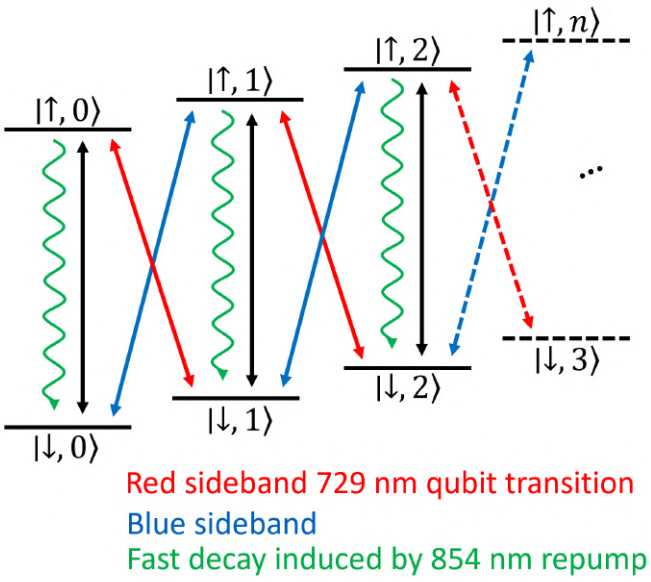

Fig. 3.3: Schematic of the laser pulses used to decrease the motional energy of an ion using sideband cooling. The red detuned laser excites the ion into a higher electronic state but lower motional state. After which it can naturally decay into a lower electronic state or induced by the repump laser [11].

3.2.4 Laser induced transitions

Having achieved sufficient cooling of the ion, it becomes feasible to proceed with the actual quantum operations. The $^{40}Ca^{+}$ ion traps developed within this research group [12] employ optically induced transitions, meaning the valence electron of an ion can be transferred between two distinct qubit states utilising lasers. For $^{40}Ca^{+}$ ions, one of the $4S_{1/2}$ states serves as the electronic ground state, denoted as state 1. To transfer the ion into its second qubit state, referred to as state 0, a laser with a wavelength of 729 nm is utilised. The $5d_{5/2}$ metastable state is chosen for the 0 state due to its potentially extended lifetime, surpassing a second. In theory, the 1 state could be held indefinitely if external disturbances, such as magnetic fields or gas particle collisions, did not introduce heating. However, such ideal conditions are seldom encountered in practice. For an exact description of laser induced operations in $^{40}Ca^{+}$ refer to "Coherence of qubits based on single $^{40}Ca^{+}$ ions" by Schmidt-Kaler et. al [13].

The quantum computing setup involving $^{40}Ca^{+}$ ions calls for the implementation of four distinct wavelengths, each serving specific roles. The table 3.1 below provides a comprehensive summary of these wavelengths and their respective functions. Additionally, the figure 3.4 illustrates all the relevant electronic transitions of the Ca qubit.

Tab. 3.1: An overview of the lasers needed to implement the quantum operations as well as cooling cycles in a $^{40}Ca^{+}$ based quantum computer.

Laser wavelength (nm)	Laser function
397	Cooling and readout
729	Optical qubit control
854	Repump for qubit
866	Repump laser for cooling and readout

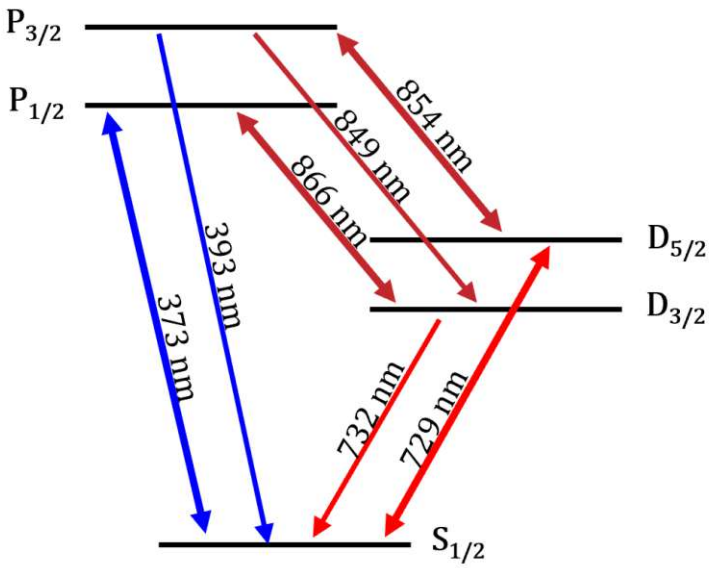

Fig. 3.4: This diagram shows the energy states of a $^{40}Ca^{+}$ ion as well as the used laser wavelengths (denoted by double tipped lines) and the emitted fluorescence of the ion (denoted by single tipped lines) [14].

3.3 Optical integration-Photonics

Until recently, with only a few exceptions, the laser addressing setup for an ion trap was typically positioned outside of the cryostat on optical racks and tables [15]. However, this conventional design encounters an inherent issue - the limited peripheral real estate. While the area accessible for trapping ions scales with the square of the trap's edge length, unfortunately, the perimeter scales linearly. As a consequence, when scaling the number of ions, severe constraints arise in

peripheral space. To overcome this challenge and gain a competitive edge in the scaling race during the Noisy Intermediate Scale Quantum (NISQ) era of quantum computing, one of the most significant improvements lies in the strategic integration of as many components as possible. By streamlining the setup and enhancing component integration, researchers can optimise the use of available space and make significant strides in scaling up ion trap-based quantum computing systems [16].

However, integration of all the necessary electronics and optics for ion manipulation poses considerable challenges, even on a macroscopic scale. Scaling up the number of ions that can be trapped and utilised for quantum computations has recently been a major focus in academia. A significant breakthrough was achieved by transforming the traditional macroscopic Paul-trap displayed in figure 3.1 to a flat chip design, where RF and DC electrodes are relocated onto a single flat plane. This innovative approach enables trapping more ions within a smaller volume, enabling the potential for smooth ion movement between various operational zones [17].

Although the transition from macroscopic Paul traps to flat chip designs offers numerous advantages, arguably the most crucial is the integration potential with complementary Metal-Oxide Semiconductor (CMOS) and Micro-ElectroMechanical Systems (MEMS) manufacturing technologies. By tapping into the world of CMOS and MEMS, ion traps benefit from incredible process control and manufacturing accuracy [18]. Consequently, not only does this advancement reduce manufacturing time and costs, thereby improving the economic viability of researching ion traps, but it also paves the way for the seamless integration of optics and electronics into the ion trap chip, leveraging well-established technologies. The semiconductor industry's reliance on stringent manufacturing specifications also enables the construction of ion traps with heightened precision and reproducibility. Furthermore, the shrinking feature and component sizes, often to the order of nanometres, make CMOS and MEMS technologies ideal for integrating numerous essential components, facilitating the development of compact ion trapping chips. Considering the necessity of having thousands of ions to achieve competitiveness with classical computing, the significance of this innovation becomes evident. An example of how a CMOS or MEMS manufactured ion trap could look is displayed in figure 3.5 [4, 19, 20].

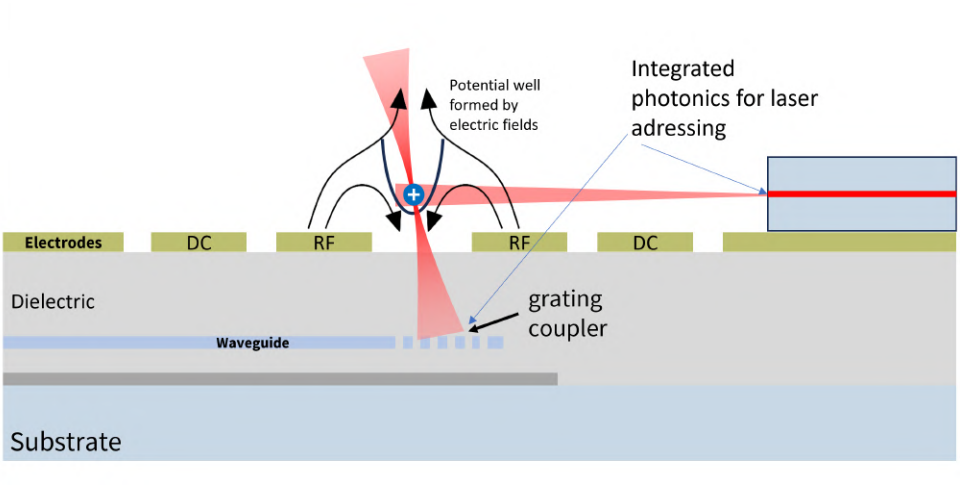

Fig. 3.5: An illustration of what a potential CMOS or MEMS fabricated ion trap could look like. Using lithographically manufactured electrodes and implementing optical addressing in two variations; a monolithically fabricated grating coupler and a waveguide written in glass [14].

The significance of miniaturising and integrating the optical addressing of trapped ions extends beyond space-saving considerations. Free space optics also often involve intricate and cumbersome setups. Moreover, since these optics are positioned outside of the cryostat, they are susceptible to temperature-induced drifts and differential vibrational modes illustrated in figure 3.6, which can lead to displacements of the laser's focal point. Consequently, these factors not only demand time-consuming maintenance efforts to prevent or manage but also impose limitations on the performance control of coherent processes. Furthermore, beam pointing errors can give rise to additional challenges, such as stray light-induced charging of surfaces. The most effective solution to address these concerns involves relocating all optical beam delivery components into the trap itself [21].

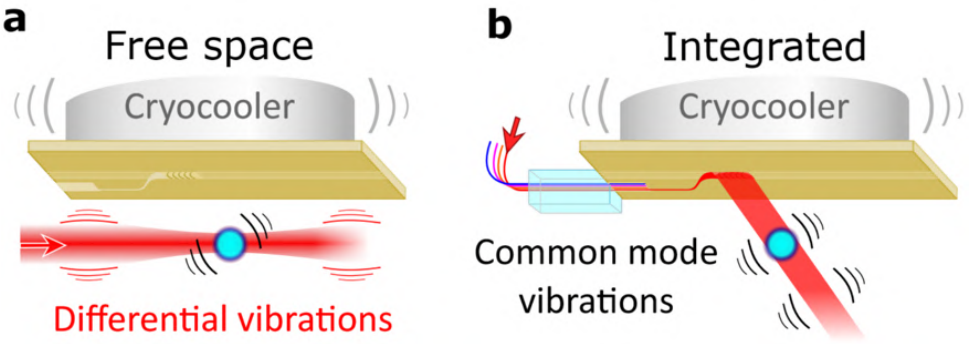

Fig. 3.6: Depicted is an example of the vibrational mismatch that can happen in an ion trapping set up. Example a) shows the scenario where ion, laser and trap vibrate at different frequencies and amplitudes. This makes controlling the ion very difficult. In example b) due to being physically coupled the trap and lasers experience the same vibrations [22].

3.3.1 Optical integration

This integration of optical delivery has already been extensively documented and has even already proven successful in performing high-fidelity gate operations [23]. This implementation involves the use of diffractive gratings as outputs, coupled with optical waveguides to precisely focus laser light onto an ion's specific location. By optimising the size and material refractive indices of the waveguides, single-mode propagation can be achieved, ensuring precise optical delivery. However, a critical complication arises due to the specific material requirements for optical components. As these components must be transparent in the visible spectrum, the default choice of material is a dielectric, which inherently presents challenges to the stability of a trapped ion [20, 24].

3.3.2 Dielectric noise from integrated optics

The presence of dielectrics has been predicted, simulated, and experimentally confirmed to introduce unwanted noise into the system by adversely affecting the electric field around trapped ions. This detrimental impact occurs through two main mechanisms. Firstly, dielectrics inherently possess stray charges that can disrupt the ion's trapping potential. Secondly, they are particularly susceptible to generating electric field noise through various mechanisms, leading to ion heating. Dielectric stray fields negatively influence the ion by altering the potential well in which it is trapped. These stray fields can be induced simply by the surface structure of the dielectric or implanted electrons. Additionally, when subjected to electric fields, dielectrics can become polarised, resulting in net positive or negative charges on their surface [25]. Furthermore, beyond

the dielectric itself being a source of noise, the oscillation of the trapped ion above the dielectric surface can induce oscillations in the dielectric material, inducing feedback heating for the ion. While the stray field noise occurs on a timescale of seconds to hours the heating noise is much faster occurring on the order nano- to microseconds. Both noise components can theoretically be compensated, but this is a tedious and difficult process. Since, even at a distance of 600 µm the dielectric's influence on the ion remains significant and ions are often closer than this to optical gratings or other optical components, a trapped ion will be subjected to a strong influence of noise [26–28].

3.3.3 Potential solution to dielectric noise

Similar to how free charges in the ionosphere can reflect radio waves and create a shield against certain electromagnetic frequencies, a similar concept can be applied to achieve shielding of ions from dielectric noise. By incorporating electromagnetic shielding, the induced oscillations from and in the dielectric can be effectively prevented. One of the simplest and most efficient methods to achieve this is by coating the optical components with a metal. The Debye length, calculated using the Thomas-Fermi screening approximation (see equation 3.1), indicates that the electric field decays over distances on the order of angstroms in metals due to electron shielding effects. However, metals, being opaque, are commonly unsuitable for integrated optics. Fortunately, there is a class of materials known as transparent conductors (TCs), which, as the name implies, possess both electrical conductivity and optical transparency. This property allows them to act as shields and effectively dissipate charges while still permitting visible light to pass through [29, 30]. In the Thomas-Fermi screening approximation,

$$
\begin{aligned}
k_0^2 &= 4\pi e^2 \frac{\partial n_0}{\partial \mu}, \\
\frac{k_0^2}{k_\mathrm{F}^2} &= \frac{4}{\pi}\frac{me^2}{\hbar k_\mathrm{F}} = \frac{4}{\pi}\frac{1}{k_\mathrm{F} a_0} = \left(\frac{16}{3\pi^2}\right)^{2/3}\left(\frac{\mathrm{r_s}}{\mathrm{a_0}}\right); \\
k_0 &= 0.815\, k_\mathrm{F}\left(\frac{r_\mathrm{s}}{a_0}\right)^{1/2} = \frac{2.95}{(r_\mathrm{s}/a_0)^{1/2}}\text{Å}^{-1}.
\end{aligned}
\tag{3.1}
$$

Here k_0 is the Thomas-Femi wave vector, m is the electron mass, e is the electron charge, $\frac{\partial n_0}{\partial \mu}$ the density of levels at the Fermi energy and k_F is the Fermi Energy wave vector.

To understand how a material can fulfil these seemingly mutually exclusive properties we must delve into the realm of solid-state physics, specifically focusing on the intricate interplay between optical transparency and electrical conductivity in various materials.

Chapter 4

Understanding material conductivity and optical transparency

4.1 Free electron conductors

Nearly all defining characteristics of metals can be attributed to a common property known as the "free electron gas." This unique phenomenon arises from the formation of metal bonds which create unbound valence electrons that move relatively unencumbered through the solid. These, for all intents and purposes, unbound electrons are responsible for crucial aspects such as heat capacity, opacity, and electrical conductivity in metals. The simple assumption, the Drude model, enables remarkably accurate predictions of these metal properties. In the derivation of conductivity, one establishes a foundation for examining the key parameters influencing conductivity metrics [31]. It becomes evident from this derivation that the high numbers of free electrons, their minimal mean scattering time and low effective masses are key players in determining a metals core characteristics [32]. The electrical conductivity σ is defined by $j = \sigma E$ so by

$$\sigma = \frac{\eta e^2 \tau}{m}, \tag{4.1}$$

where n is the number of free electrons, e is the electron charge, τ is the mean scattering time and m the mass of an electron.

4.2 Optically transparent metals

In metals, the absence of a band gap, visualised in figure 4.1, allows for continuous electron energy states, enabling incoming photons to excite the free electrons without any energy threshold requirements. These free electrons exhibit behaviour akin to a plasma and can be readily excited by electromagnetic waves. The process of photoexcitation, wherein an electron is raised to a higher energy state and subsequently decays back to its original state, occurs on an ultrafast timescale, and spans an extensive spectral range. As a result, metals emit a spectrum that closely mirrors the wavelength of the incident light. This intrinsic property makes metals excellent reflectors of radiation throughout the electromagnetic spectrum, endowing them with their characteristic metallic lustre and rendering them ideal for mirror applications [32].

Moreover, due to the electron behaviour resembling that of a plasma, metals possess a distinctive plasma frequency. Beyond this frequency, metals become transparent to all electromagnetic radiation. As exemplified in the equation 4.2 of the plasma frequency below, at higher frequencies, typically in the terahertz (THz) range, electron motion cannot keep up with the oscillating electric field of the incoming electromagnetic radiation. Due to the absence of electron polarisation, the dielectric constant reduces to unity, resulting in the metals transparency. This transparency

phenomenon is commonly observed at low ultraviolet (UV) wavelengths for metals that closely adhere to the Drude approximation, such as alkali metals. However, noble metals exhibit interband transitions and their electrons experience relativistic effects, deviating from classical theories. This leads to unique properties, including plasmon polariton interaction and wavelength dependant characteristics which will be relevant in subsequent discussions [33, 34].

$$\omega_p = \sqrt{\frac{n \cdot q^2}{\varepsilon_0 \cdot m^*}}, \tag{4.2}$$

where ω_p is the plasma frequency, e is the charge of an electron, ε_i is the permittivity constant of the material and m^* is the effective electron mass.

Having elucidated the key factors that render a material electrically conductive and optically transparent, we can now discern the underlying challenge. The presence of free charges necessary for electrical conductivity, may exhibit behaviour reminiscent of a metals free electron plasma and thus absorb electromagnetic radiation, particularly within the visible spectrum. As listed in table 3.1, the wavelengths employed in ion trapping are considerably distant from the ultraviolet regime where certain metals could potentially become transparent. Fortunately, there are exceptions to the previously established opacity of metals, particularly when these are deposited as extremely thin films, on the order of just a few nanometres. In such thin films, the mechanism behind the metal's transparency does not involve modifying the metal's plasma frequency. Instead, it can be attributed to the minimisation of the equation 4.3 for absorption in a dielectric medium

$$A = \frac{4\pi n(\lambda)k(\lambda)}{\lambda_0} \int_0^d (\mid E(z) \mid)^2 dz, \tag{4.3}$$

where n is the refractive index, k is the absorption coefficient and E is the electric field in the material.

The presented equation 4.3 clearly indicates three key factors that can be minimised to mitigate absorption. Firstly, the thickness, a self-evident parameter, plays a pivotal role in reducing absorption, and its significance necessitates no elaboration. Secondly, the values of n and k, which are interrelated material characteristics derived from the imaginary dielectric function epsilon (ε_i), must be minimised. As these factors are inherently linked, a reduction in one will naturally lead to a decrease in the other. Due to the material dependence of n and k the optimisation falls on the selection of suitable materials. Notably, certain metals such as Cu, Ag, and Au exhibit low values of ε_i, rendering them favourable candidates for use as transparent conducting thin films. Moreover, these metals boast high conductivities, adding to their appeal for the dual functionality [35]. Further improving metal film transparency involves enhancing its homogeneity to impede the formation of islands, since these islands can induce absorption through plasmon polariton interactions. Furthermore, islands create multiple angles at which incident light may undergo total reflection [36].

4.3 Transparent semiconductors

In contrast to metals, which exhibit excellent electrical conductivity, electrical insulators represent the opposite end of the spectrum. Their electrical conductivity is significantly impeded due to the strong inhibition of electron movement, resulting in a scarcity of free electrons. Insulators are characterised by large band gaps, see schematic in figure 4.1. These gaps can only be traversed by electrons absorbing thermal or electromagnetic energy. The magnitude of the

band gap also dictates the regions of the electromagnetic spectrum through which the material remains transparent. This leads to the most prominent advantage of many insulating materials, their remarkable optical transparency over a large frequency of electromagnetic radiation. For insulators with high-energy band gaps (E_G) exceeding 3.1 eV, light in the visible spectrum lacks sufficient energy to excite electrons between bands, granting the material optical transparency in the visible spectrum. This range includes all wavelengths which are useful for $^{40}Ca^{+}$ manipulation. An illustrative example is diamond, boasting a band gap of 5.37 eV. Conversely, materials like silicon, possessing a band gap of 1.12 eV, remain non-transparent to visible spectrum photons, as these possess adequate energy to excite electrons within the material. Notably, silicon exhibits transparency to infrared (IR) wavelengths, specifically wavelengths greater than 1127 nm [29].

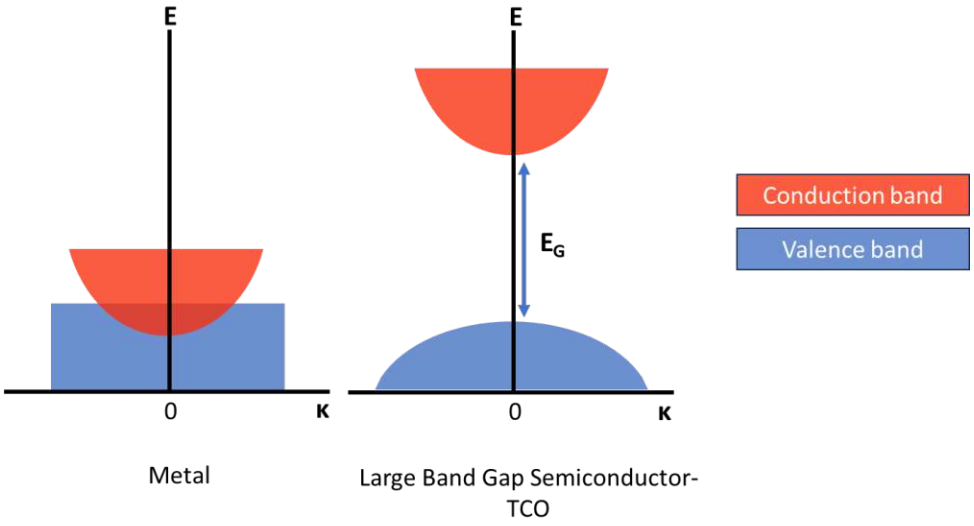

Fig. 4.1: On the left is the band structure of a metal, with overlapping bands therefore facilitating unhindered movement for electrons. Then the band structure of a semiconductor where the precise band gap energy difference and band curvature depends on the material chosen [37].

4.4 Semiconductor doping

As previously mentioned, a material assumes the characteristics of an electrical insulator when it possesses a large enough band gap that hinders electron movement and lacks free intrinsic charge carriers. In contrast, semiconductors constitute a distinct class of materials, exhibiting a history of precise tuning of their electrical conductivity while retaining a band gap. In a single crystal semiconductor at absolute zero (0 K), its electrical conductivity is absent as electrons lack the energy required to traverse the band gap. However, upon introducing a non-zero temperature, thermal energy can induce the formation of electron-hole pairs in the conduction and valence bands, respectively. This allows for charge transfer and subsequent conductivity, albeit at low levels due to the limited available number of defects. The equation below, derived using Fermi-Dirac statistics and the density of states, predicts the quantity of charge carriers present in an intrinsic semiconductor at room temperature [38].

$$n(E) = N(E) \cdot f(E), \tag{4.4}$$

where $n(E)$ is the electron concentration at an energy E which is given by the product of $N(E)$, the density of states, and $f(E)$, the Fermi Dirac distribution function.

$$f(E) = \frac{1}{\exp\left(\frac{E-\mu}{k_B T}\right) + 1}. \tag{4.5}$$

Using the Fermi-Dirac distribution function one can then find the electron concentration in a small energy range surrounding the conduction band at $E + dE$,

$$n(E)dE = \frac{\sqrt{2} \cdot (m^*)^{3/2}}{\pi^2 \cdot \hbar^3} \cdot \frac{\sqrt{(E-\mu)}dE}{\exp\left(\frac{E-E_F}{k_B T}\right) + 1}, \tag{4.6}$$

where k_B is the Boltzmann constant, μ the chemical potential, m^* the electrons effective mass, $\hbar$ the reduced Planck constant, E_C the energy of the conduction band and E_F the Fermi energy.

Using the equations above, one can calculate that silicon at room temperature contains approximately 10^{14}cm^{-3} charge carriers. While this quantity may appear significant and enables semiconductors to exhibit conductivity orders of magnitude higher than insulators, it still remains substantially lower than that of metals. However, there exists a method to introduce additional charge carriers by doping the semiconductor with precise amounts of specific impurities. The addition of impurities to an intrinsic semiconductor transforms it into an extrinsic semiconductor, and if the doping concentration is high enough, it becomes a degenerate semiconductor. These impurities, known as dopants, augment the semiconductor's conductivity by increasing the defect density. Theoretically, any foreign atom could serve as a dopant, but it is prudent to select one with a similar ionic radius to avoid unnecessary distortion of the crystal lattice and ensure that it possesses one valence electron more or less than the substrate. In the case of silicon which can be seen in figure 4.2, the doping atoms used are phosphorous and boron. After both doping scenarios, the electrons need now only overcome an energy barrier of 0.045 eV to transition to the nearest conduction energy level. This allows charges to move with significantly reduced energy requirements, merely 0.045 eV compared to 1 eV [37].

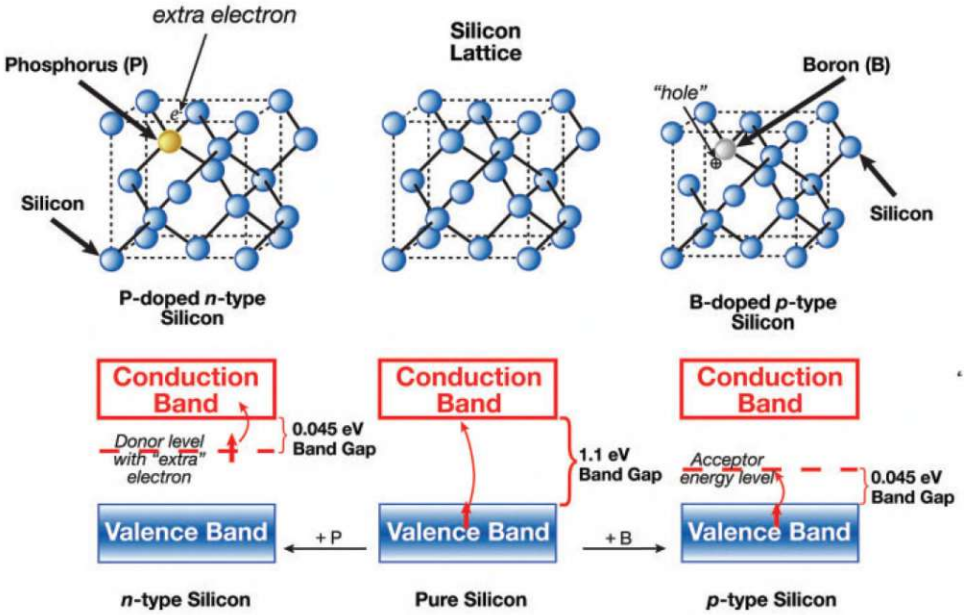

Fig. 4.2: An example of the effect of doping in silicon on both the crystal structure and the band structure [39].

The conductivity of a semiconductor can be described using the following equation:

$$\frac{1}{\rho} = \sigma = n \cdot \mu \cdot e, \tag{4.7}$$

Here, ρ is the resistivity, σ the conductivity, n the number of electrons, μ the electron mobility and e the electron charge.

In the case of a degenerate semiconductor, only the majority charge carrier concentration become relevant due to the significant disparity between the concentrations of holes and electrons. As a result, only one concentration parameter is necessary. The conductivity is then mainly determined by the mobility μ with the following expression:

$$\mu = \frac{e\tau}{m^*}, \tag{4.8}$$

where μ is the mobility τ is the mean time between collisions and m^* is the effective mass.

The two main factors that influence the mobility are the effective mass and the mean free path. The effective mass is solely determined by the material choice as it represents the second derivative of the band structure, specifically the curvature of the conduction or valence band. A low effective mass enhances the conductivity, making steep bands more desirable. Additionally, the mean free path, especially at high doping concentrations, is predominantly influenced by ionised impurity scattering and grain boundary scattering, as described by a modified Matthiessen's rule below in equation 3.8. The film's thickness also plays a critical role, as at thicknesses under 100 nm, electrons experience high scattering at the surface boundaries [40].

$$\rho = \rho_{\text{Grain-boundaries}} + \rho_{\text{Phonon}} + \rho_{\text{Impurity}} + \rho_{\text{Surface scattering}} \tag{4.9}$$

4.5 Transparent conductive oxides

Using the knowledge we have gained about conductivity and transparency, we can aim to design the ideal transparent conductor for ion traps. This requires a material with a band gap of approximately 3.2 eV (thus transparent to wavelengths up to 390 nm) and an electron gas to act as an electromagnetic shield. However, as previously discussed, both of these characteristics typically exclude each other. Nevertheless, degenerate semiconductors offer a viable compromise, as they can approach the conductivity levels of metals. Thankfully, certain transition metal oxides with band gaps exceeding 3.2 eV exist, and they can be doped to exhibit degenerate semiconductor conductivity properties. Nevertheless, we must be cautious not to excessively increase the carrier concentration, surpassing $10^{21}\,\mathrm{cm}^{-3}$, as this would shift their plasma frequency into the infrared regime. On top of this, these transparent conductive oxides (TCOs) also have steep band structures allowing for low effective electron masses. Additionally, to prevent photon absorption from exciting electrons from the conduction band minimum to higher conduction bands, a second significant energy gap above 3.2 eV here is essential [41].

The relevant transition metal binary oxides for this application are described using the general stoichiometric formula $M_xO_y : D$, where M_xO_y represents the transition metal oxide and D the doping element. Some of these oxides may possess a band gap of less than 3.1 eV, which however can be enlarged through degenerate doping, by utilising in the Moss-Burstein effect. This effect increases the apparent band gap of a semiconductor due to degenerate doping, with electrons occupying the conduction band and therefore pushing the absorption edge to higher energies. The precise mechanisms responsible for electron conduction in these materials, apart from doping, remain unclear, likely involving a combination of factors such as oxygen vacancies and proton interstitials. Interestingly, only n-type doping is feasible in these materials to fulfil the required conductivity and transmittance criteria. Attempts to p-type dope the standard TCOs encounter issues, as their valence band is composed of oxygen 2p states, which when doped leads to the formation of strong polarons that inhibit conductivity. Moreover, they feature low dispersed valence bands, resulting in high effective masses for holes [42, 43].

A comprehensive overview of the theoretical considerations for designing the essential films has been presented, emphasising their role in enhancing today's trapped ion quantum computers. We now delve into the investigative and preparatory steps taken to study these films.

Chapter 5 introduces the test setup for electrical and optical analyses, outlining the necessary requirements for accurate film characterisation. Identified shortcomings and recommended improvements will also be discussed.

In Chapter 6, we explore metals, metal alloys and metal-like compounds, evaluating their potential as shielding layers. On top of this, wetting layers of Al_2O_3 are introduced and their role in improving the percolation of gold films is investigated. Chapter 7 focuses on the influence of different deposition techniques on sidewall and high aspect ratio coverage.

Chapter 8 introduces the material class of transparent conducting oxides, with a specific examination of Al:ZnO's potential as a dielectric shielding layer.

Finally, Chapter 9 presents a conclusive summary of the examined films, comparing them with other conventional and novel materials discussed in current literature for similar applications.

Chapter 5

Evaluating the optical and electrical properties of thin films

All materials describe from here on as Borofloat can be more exactly defined as a 500 µm thick BOROFLOAT® 33 sample obtained from the SCHOTT AG. All thin films were deposited on 8 inch-200 mm Borofloat wafers and their properties were measured at ambient conditions unless stated otherwise.

5.1 Evaluating the electrical sheet resistance using the Four-Point-Probe method

To properly assess the suitability of films for shielding ions from dielectric charges, it is crucial to quantify their sheet resistance, as this directly influences the material's ability to shield and transport created charges. Various methods can measure sample resistivity, such as variable probe spacing [44], Van der Pauw and the four-point probe (4PP) method [45].

The four-point probe method was chosen for this study due to its ease of needle (probe) placement and the possibility for a non-destructive measurement of entire 200 mm wafers without having to account for geometric considerations. Additionally, the 4PP method allows for precise measurements of semiconductors or low-conductivity films, as the needle-semiconductor contact can be excluded from the resistivity measurement. The procedure involves placing four needles spaced evenly apart in a line on the sample surface, with current passing between the outermost needles and the floating voltage measured between the inner two needles. By using the measured voltage and applied current, the resistivity of the thin film can be accurately determined, as demonstrated in the equations in 5.1. For the equations to be valid in accurately measuring the resistance of a sample it must fulfil the following boundary conditions [45].

1. The resistivity of the sample must be isotropic, and this is the case with our samples as we are measuring amorphous or polycrystalline films.
2. The probes lie in a straight line and are evenly spaced on a flat surface.
3. The distance from a given needle to an edge should be at least five times the needle spacing. All samples were larger than 1 cm by 1 cm, and since we had a probe spacing of 250 µm, this was always guaranteed.
4. The thickness of the film should also be very small compared to the probe spacing, and the ratio of the film thickness to needle spacing should be smaller than 0.5. This allows us to measure films accurately up to 125 µm thick [45].

With all boundary conditions satisfied, the samples were subjected to measurements at room temperature using a Cascade 30018 needle prober by applying a current sweep from −1 mA to 1 mA and recording the corresponding voltage readings.

Presented in figure 5.1 is an example of the I-V curve obtained through the 4PP measurement of a thin Al:ZnO (AZO) film. The gradient resulting from the linear regression can be directly inserted into the equation 5.1, enabling the calculation of the sheet resistance in ohms per square (Ω/□). The sheet resistance can be converted to the resistivity using the equation 5.1 below, however the sheet resistance as a figure of merit is preferred. Since resistivity does not purely capture a film's essential resistance but skews it to include the film's thickness. Occasionally, to emphasise certain properties, the term "conductivity" may be used instead of "resistivity", which is merely the reciprocal value of the resistivity in equation 5.1.

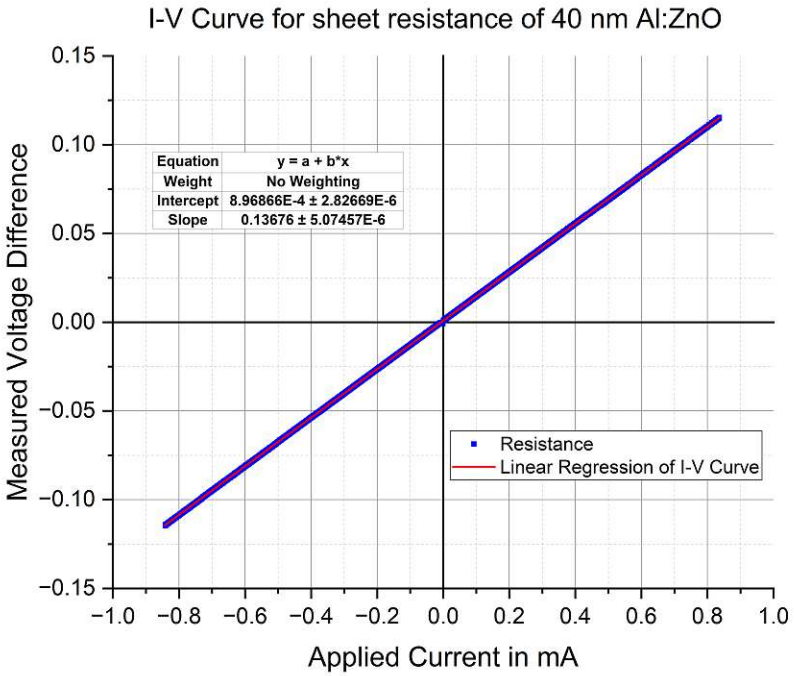

Fig. 5.1: Displayed is the I-V curve that is obtained as a result of plotting the measured voltage and the applied current through the 4PP setup. Since the current is displayed in mA the resistance is 136.8 Ω. Using the equations below one can calculate a sheet resistance of 617 Ω/□.

$$\begin{aligned} R_S &= \frac{\pi}{ln(2)} \cdot \frac{\Delta V}{I} \\ \rho &= R_S \cdot d \\ \sigma &= \frac{1}{\rho} \end{aligned} \tag{5.1}$$

Where R_S is the sheet resistance, ΔV the measured voltage, I the applied current, d the film thickness in cm, ρ the resistivity and σ the conductivity.

To mitigate the possibility of surface effects influencing the resistance measurement, the probe spacing was deliberately varied on a sample. The consideration of thin film effects would have been necessary if the probe spacing had a substantial impact on the resistance values. However, due to the consistent and homogeneous results obtained which can be seen in figure 5.2, thin film effects were ruled out.

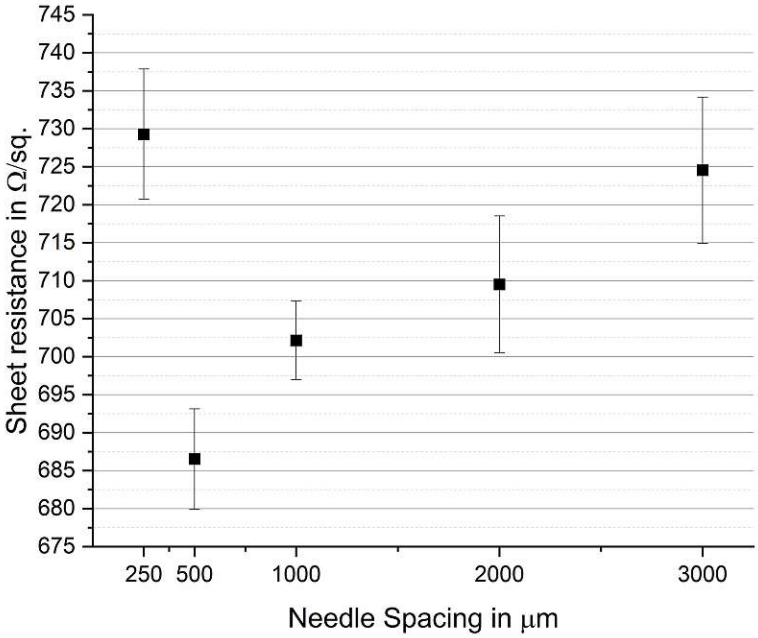

Fig. 5.2: An overview of the sheet resistance of the same sample with different needle spacings during a 4PP test. Although there is a large discrepancy between the resistance values the overall lack of a trend indicates little to no dependence of probe spacing on the resistance.

5.2 Evaluating the wavelength dependant optical transmission

To accurately analyse the transmission spectrum through the deposited film on a Borofloat substrate, we utilised a 10 W halogen lightbulb as a light source. To enhance the light output and directionality, the lamp was enclosed in a box coated with aluminium. To minimise thermal effects this setup was positioned outside the sample box, which contained the samples and the photospectrometer, a rendering of the setup can be seen in figure 5.3.

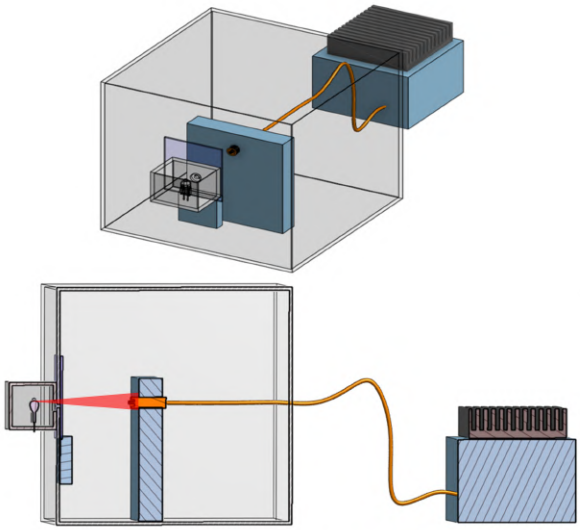

Fig. 5.3: An overview of the setup used to measure the transmittance of different samples. The box was made of an opaque matte black polymer. A SMA 905 0.22 numerical aperture single-strand multimode optical fiber was used for light capture and delivery to the LR1 – ASEQ Instruments Broad spectral range photospectrometer.

The complete setup was securely mounted on a tabletop to mitigate vibrations, which were found to negatively impact the measurement repeatability by affecting the fibre optics' mechanical stability. Prior to conducting measurements, the entire apparatus was given a 30-minute warm-up period. This allowed any water present in the light bulb box to evaporate, preventing condensation on the substrate. Additionally, this warm-up period allowed for the slight initial deviation in the lamp spectrum to be eliminated as the tungsten wire reached its optimal operating temperature. The measured spectrum from the halogen bulb seen in figure 5.5 was consistent with those reported in literature [46].

The photospectrometer utilised in this setup incorporated a Toshiba TCD1304DG linear array-charge coupled device (CCD) for detecting transmitted photons [47]. The choice of this device implies the usage of a metal-oxide-semiconductor (MOS) structure to register impinging photons which is illustrated in figure 5.4. The MOS structure facilitates the detection of incoming photons as electrons generated through the photoelectric effect in doped epitaxial silicon. These electrons are captured and retained in a potential well produced by applying a gate voltage to the metal, biasing the MOS structure. After a certain exposure time, the electrons accumulated in the potential well can be extracted as a current proportional to the intensity of the interacting photons with the MOS pixel. However, this setup only captures the spatial intensity of incoming photons. To obtain a wavelength-dependant intensity profile, a diffracting prism or grating can be introduced between the MOS pixel and the incoming light. To quantify the number of electrons in a well, the potential is shifted to move the electrons along into the next well and so forth until they reach the output, where the precise number of electrons can be determined [48].

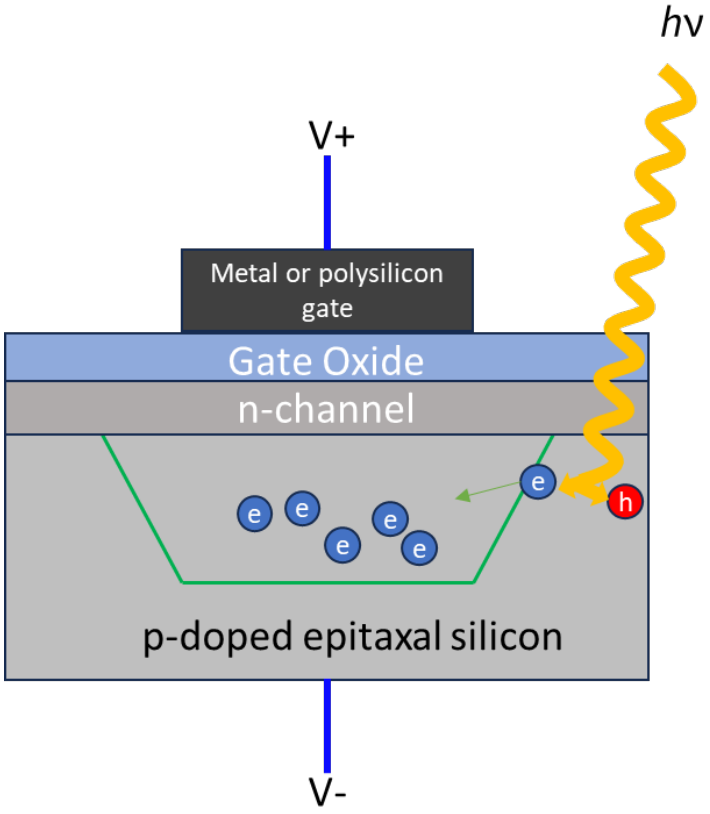

Fig. 5.4: Overview of the structure of a CCD pixel, many of these can be fabricated side by side to achieve high resolution photon read outs.

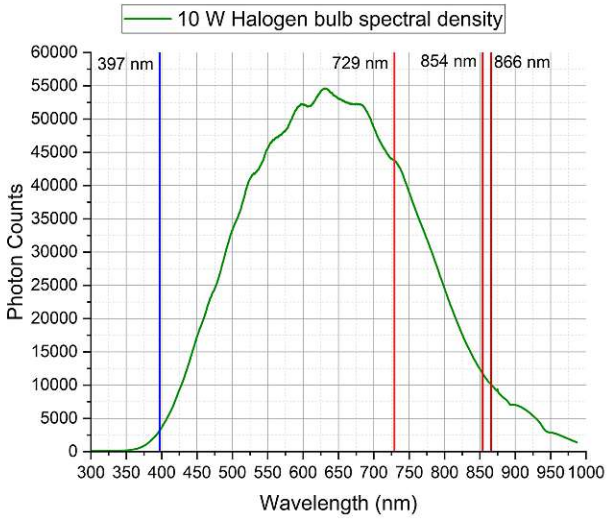

Fig. 5.5: The unfiltered spectrum of the 10 W halogen bulb that was used for the transmission experiments. As was previously described although this bulb worked to produce most wavelengths in the visible regime it lacks UV components which may be of interest for future experiments.

To measure the transmission of the deposited film, first the initial spectrum of the Borofloat substrate was recorded, observing a maximum detector count of approximately 60,000. By adjusting the exposure time to achieve this count in every measurement, not only was the noise minimised, but even with variations in the optical fibre's distance from the source during different experiments, the measured spectra remained consistent. Once established as the baseline, the coated Borofloat sample was recorded. The transmission values of the pure Borofloat substrate in this setup are presented below. As anticipated with the halogen bulb, the spectrum displayed considerable noise below 400 nm and above 900 nm. However, this region encompasses all the necessary wavelengths for $^{40}Ca^{+}$ and therefore is not deemed as a problem.

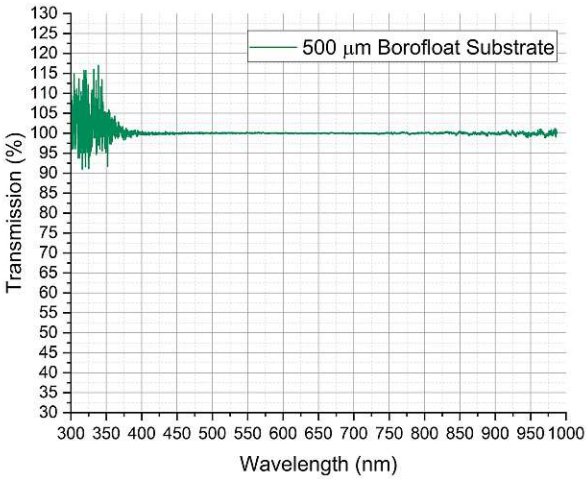

Fig. 5.6: The transmission spectrum of a pure Borofloat wafer that was set to 100% transmission. Visible here is how strong the noise becomes below 375 nm.

5.3 Investigating the shortcomings of the optical setup

Ensuring the reproducibility of a transmission measurement was a crucial aspect of our setup. To investigate this, multiple measurements of the same sample (1.55 µm Al:ZnO on 500 µm Borofloat) were conducted over several weeks and the obtained spectra plotted, as depicted in figure 5.7. Naturally, the standard deviation of our measurement apparatus varied with the wavelength measured, primarily due to the presence of increased noise at different points in the spectrum. Nonetheless, the resulting standard deviation remained sufficiently low across all relevant wavelengths, enabling qualitative analysis of the results. The observed discrepancies between measurements can be attributed to several factors. Firstly, the natural drift of the electronics, particularly the photospectrometer. Additionally, as the sample is inherently inhomogeneous, precisely measuring the transmission of the exact same area during each run proved extremely challenging and could also contribute to the deviations. Despite efforts to ensure the sample's perpendicular alignment to the light beam, minor deviations might also have occurred, impacting the measurements.

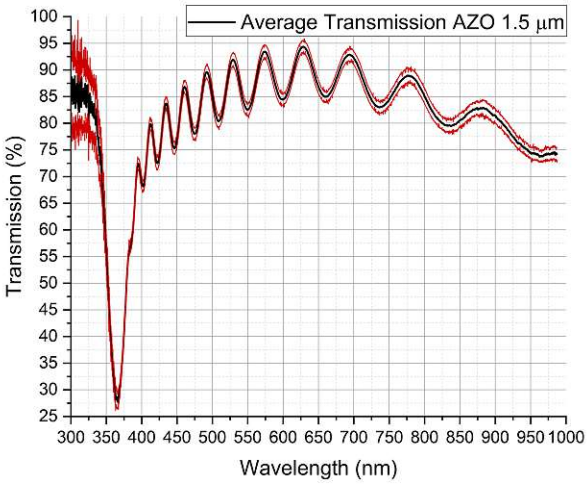

Fig. 5.7: Using 24 measurements of the same AZO sample over the period of some weeks the standard deviation and therefore the reproducibility of the experiment was checked. The red bands are the plotted standard deviation and the black line the average of all the measurements. Although this reproducibility may be much lower than for commercial systems the qualitative analysis is still useful.

To ensure the congruence between the acquired data and theoretical expectations, two sets of experiments were conducted on the coated samples. In the first set, the transmission of the substrate was measured followed by the film, while in the second set, the order was reversed and the film was measured first and then the substrate. The order of measurement, whether the film or the substrate was measured first, should not influence the results, and this assertion was confirmed in the experiments. As illustrated in the spectrum in figure 5.8, there exists minimal disparity between the two transmission curves. Any observed variation can be attributed to the inherent fluctuations of the setup, that were previously outlined. For these experiments, 500 µm Borofloat coated with 45 nm TiN was used.

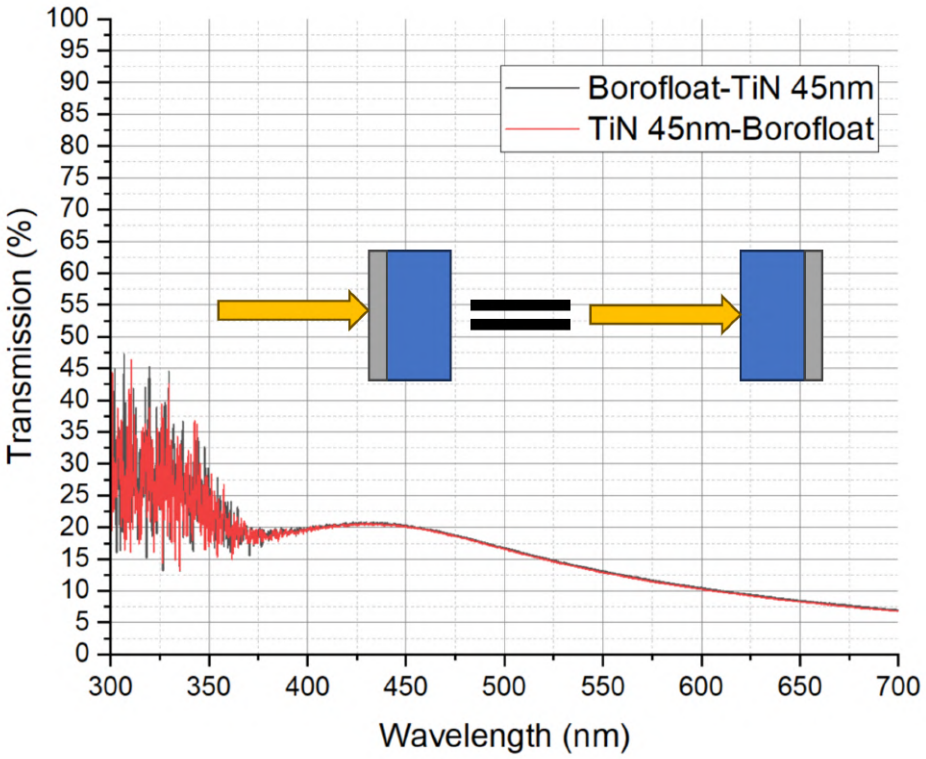

Fig. 5.8: Measuring the abelian properties of the light transmission and absorption through the sample system shows little to no change.

The setup employed in this study, although suitable for qualitative experiments, does not offer quantitative measurements. Considering the use of the Fresnel equation for perpendicularly incident light in equations 5.2, 5.3 and the known refractive index of Borofloat wafer (1.4714) [49] at 587.6 nm, the theoretical reflection losses amount to 7.27%. This implies that under the assumption of no light absorption and purely reflective losses, the transmission at 587.6 nm should be approximately 92%. However, the measurements yielded a transmittance of roughly 95%. The reflectance of s-polarised light is

$$R_{\mathrm{s}} = \left| \frac{Z_2 \cdot cos\theta_{\mathrm{i}} - Z_1 \cdot cos\theta_{\mathrm{t}}}{Z_2 \cdot cos\theta_{\mathrm{i}} + Z_1 \cdot cos\theta_{\mathrm{t}}} \right| \tag{5.2}$$

while the reflectance for p-polarised light is

$$R_{\mathrm{p}} = \left| \frac{Z_2 \cdot cos\theta_{\mathrm{i}} - Z_1 \cdot cos\theta_{\mathrm{t}}}{Z_2 \cdot cos\theta_{\mathrm{i}} + Z_1 \cdot cos\theta_{\mathrm{t}}} \right| \tag{5.3}$$

Where θ_{t} is the angle of transmittance and θ_{i} angle of incidence of light through/onto the film and Z the wave impedance. The high reproducibility of the acquired data, coupled with the deviation from theoretical expectations, suggests the presence of systematic errors in the measurements. These errors may be attributed to stray light reaching the detector and reflections from the apparatus surfaces. To mitigate these issues, several improvements can be implemented, such as applying an absorbing coating like Vanta Black$^{\mathrm{TM}}$ to the inside of the test setup, introducing lenses between the sample and the detector and incorporating a collimator or collimated light source to reduce stray light which are visualised in figure 5.9.

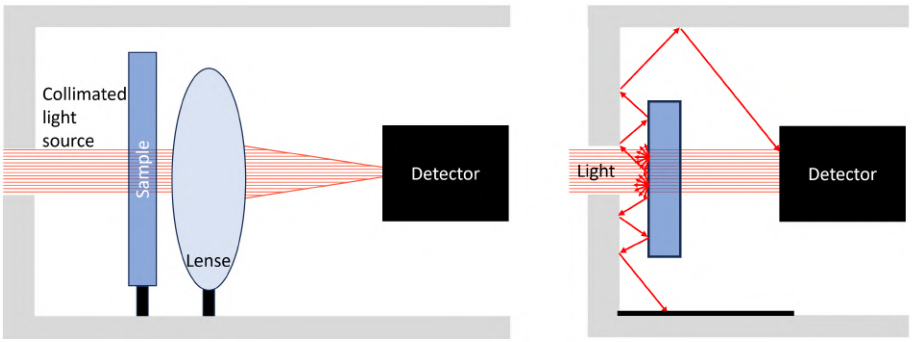

Fig. 5.9: These schematics show which improvements can be made in order to reduce the noise of the system. On top of this it may also prevent scattering issues as well as light collection which were thought to be the biggest deviation contributors to the theoretical values.

Additionally, evaluating the transmission properties of the film alone presents challenges. This is due to the way that the transmission was calculated by the photospectrometer. First the spectrum of a Borofloat wafer was captured and set as a background, 100% transmission. This accounted for the following three losses which for clarity are also displayed in figure 5.10: 1) reflection between the air and Borofloat 2) absorption in the Borofloat and finally 3) reflection between the Borofloat and the air. Afterwards, when a sample was measured, the counts were referenced to the previous Borofloat spectrum. This left one with missing interfaces, namely the interface of the film back out to the air, additionally the Borofloat-air interface was replaced by the Borofloat-film interface. Leaving some interfaces unaccounted for, made it impossible to precisely calculate losses from the film alone. Utilising the wavelength-dependant refractive index could potentially address this issue, but such data is not available for all materials. It is crucial to highlight that the primary focus of this study was not solely to scrutinise the optical properties of various thin films. Rather, the main objectives were to investigate different film possibilities and their integration into current ion trap designs, assess their compatibility with CMOS capabilities and characterise the most promising candidates' conductivity as well as qualitative optical properties.

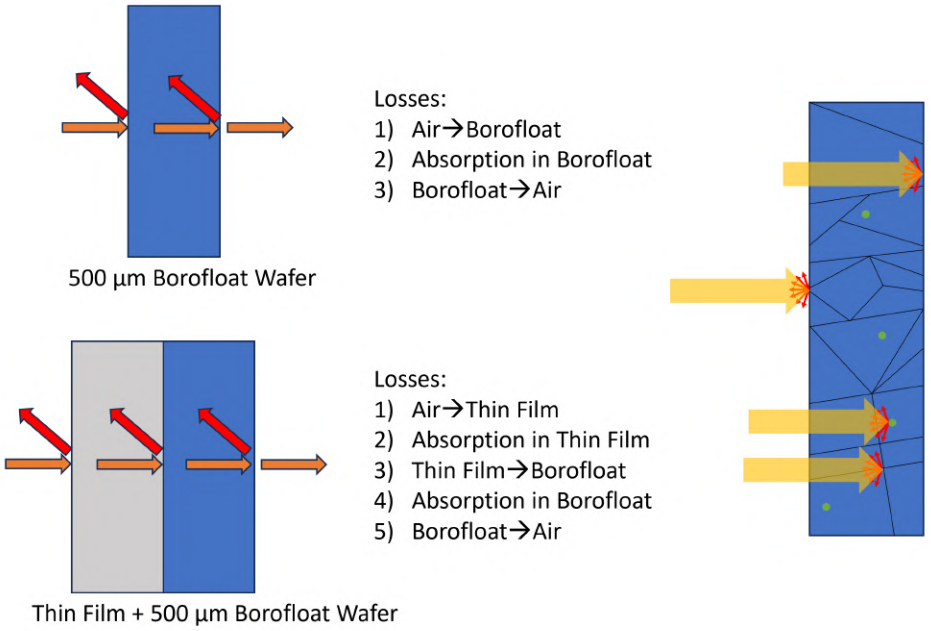

Fig. 5.10: In these schematics the different loss contributors for the Borofloat and Borofloat with film are described. These losses are the macroscopic losses but there will be further smaller losses induced by defects in the substrate or film as well as scattering losses.

Chapter 6

Investigation of thin film metals as TCs

Given the successful production of thin film metals with comparable conductivities to TCOs, it is worth investigating their use in this application further. On top of this, the deposition of metals is relatively simple and can be achieved using thermal evaporation or sputter deposition. Among the preferred metals, gold stands out due to its suitable dielectric function, widespread availability and compatibility in the fabrication process. Another material of interest, though classified as a ceramic, is titanium nitride (TiN), chosen for its long-standing use in CMOS and MEMS technologies, ensuring smooth process integration. Additionally, two alloy films, Pd-Au and Pd-Pt, were tested based on literature recommendations suggesting good transparency and conductivity characteristics for thin platinum films [50]. Furthermore, all selected materials possess high work functions, posing no threat of unwanted charges on the surface near the ion through the photoelectric effect. Table 6.1 summarises the samples investigated.

Tab. 6.1: An overview of the different metals and metal like materials that were deposited as well as their thicknesses and deposition method.

Material	Thickness in nm	Deposition Technique
TiN	13	Thermal Evaporation
TiN	24	Thermal Evaporation
TiN	34	Thermal Evaporation
TiN	45	Thermal Evaporation
Au	11	Thermal Evaporation
Au	14	Thermal Evaporation
Pd/Pt	15	Magnetron Sputtering
Pd/Au	13	Magnetron Sputtering

6.1 Transmission and electrical characterisation of TiN

TiN finds wide application in industrial CMOS fabrication, serving as a conductive material for electrodes and as a diffusion barrier. It has been selected for these roles due to its conductivity, which is comparable to that of most metals, despite its classification as a ceramic compound in theory. However, it should be noted that due to it being a chemical compound, comparing the properties measured here to literature values can be challenging. Since the characteristics of a TiN film are highly dependant on factors such as its stoichiometry, deposition method, partial pressure of precursors and temperature during fabrication [51, 52].

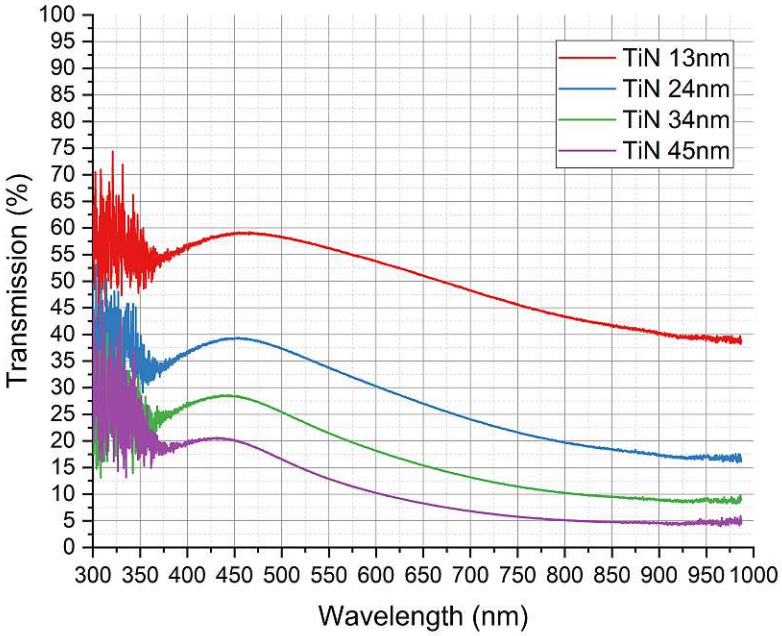

Fig. 6.1: A comparison of the different transmission spectra of TiN films. These films exhibit similar optical properties, with higher losses observed in the IR region compared to the UV range. This observation is in accordance with the predictions made by the underlying theoretical model of bulk absorption modes.

The transmission spectrum in figure 6.1 indicates a slight wavelength dependency for TiN, with higher transmission observed in the 400-500 nm range. Its golden colour as a thin film already suggests a similarity in absorption spectrum to other metals of the same colour, such as gold. The overall spectrum shape can be explained by considering the bulk absorption modes of TiN, which can be approximated using the dispersion relation. Furthermore, as expected from equation 4.3, transmission decreases significantly with increasing film thickness [53].

$$\omega = \frac{kc}{\sqrt{\varepsilon(\omega)}} \tag{6.1}$$

Where k is the wavenumber, c is the speed of light and ε is the dielectric function.

The conductivity follows the expected trend as well. However, it is important to consider that the Matthiessen rule, which describes resistance in metal films, does not fully account for electron scattering at the film's boundary layers in the case of thin films. Consequently, at low film thicknesses, surface scattering losses become significant contributors to resistance, particularly in cryogenic environments where phonons are minimised [54]. The sheet resistances of the TiN thin films are summarised in table 6.2 below.

Tab. 6.2: An overview of the different sheet resistance values of the TiN samples, which drop rapidly when the film thickness increases above 20 nm.

TiN thickness (nm)	Sheet resistance Ω/□
13	109.8 ± 6.5
24	36.3 ± 1.8
34	23.4 ± 0.8
45	15.8 ± 1.07

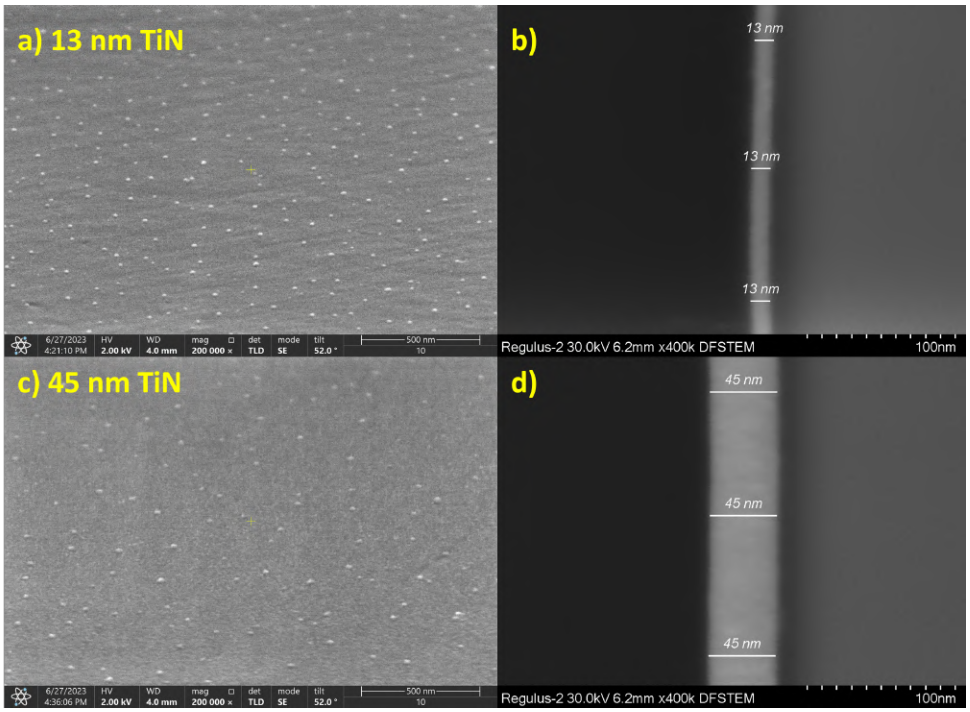

Fig. 6.2: Here the thinnest and the thickest TiN films are compared in both their surface characteristics and cross-section. An interesting feature of these films, is that they do not display different morphologies depending on their thicknesses.

The scanning electron microscope (SEM) images of the TiN surface seen in 6.2 a) and c) reveal the presence of white nodules. The contrast between these nodules and the darker TiN suggests that they possess higher conductivity than the thin film. The origin of these nodules remains unclear, and they have been reported in existing literature [55]. Despite this, both films exhibit exceptional homogeneity and show no evidence of reduced percolation. The absence of percolation at such thin thicknesses is a desirable and well-documented characteristic of thin TiN films. To precisely determine the film thickness, Transmission Electron Microscopy (TEM) measurements were employed, and two examples of such measurements can be observed in figures 6.2 b) and d) [56].

6.2 Transmission and electrical characterisation of noble metal alloys

Subsequently, PdPt and PdAu alloys were examined due to Pt and Au's prior use as thin film metals and their high electrical conductivities. The transmission spectra for AuPd and PdPt films are shown in figure 6.3. Notably, there is a substantial deviation between the two alloys, with

PdAu exhibiting nearly 20% higher transmission, especially at higher wavelengths. Interestingly, this difference persists despite both alloys having roughly the same thickness [57].

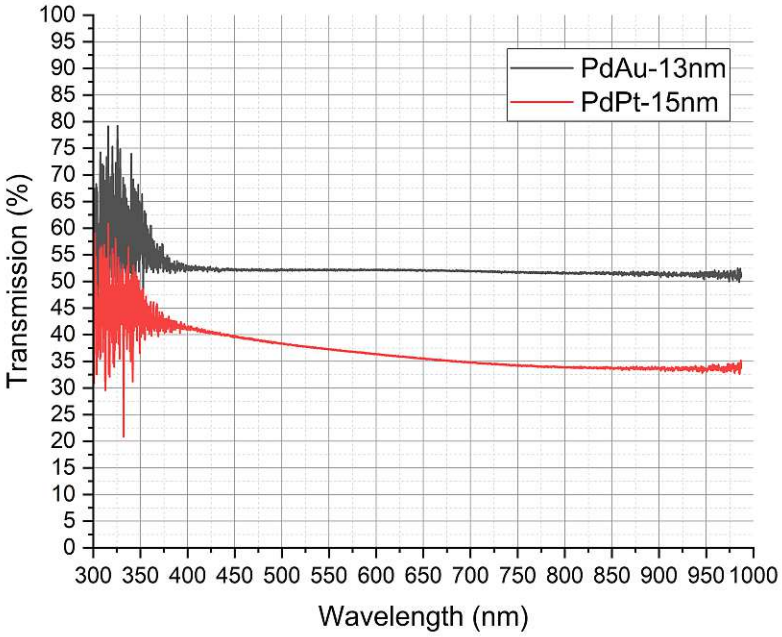

Fig. 6.3: A comparison of the transmission characteristics of the noble metal alloys. Both have few wavelength dependant features in their transmission spectrum.

Tab. 6.3: An overview of the sheet resistance values of the two alloy films. Again, like with the transmission values their sheet resistance is reflected in their surface structure.

Noble alloy thickness	Sheet resistance Ω/□
13 nm PdAu	193 ± 1.7
15 nm PdPt	136 ± 0.1

Despite the noble metal alloy films exhibiting similar transmission values to TiN films of comparable thickness, they lack the wavelength dependant transmission. The reason for these homogenous absorption characteristics is unknown but common for refractory metals. The sheet resistance values for the noble alloys in table 6.3 are significantly higher than those of TiN [58, 59], despite the bulk metals having much higher conductivities than TiN. Upon examining the surface structure of the thin films using SEM, the reason for this discrepancy becomes immediately apparent. The PdAu film displayed in figure 6.4 a) lacks homogeneity, resulting in the formation of isolated metal islands. These islands are not well-connected, with very few instances of connectivity. Consequently, the film's connectivity is extremely poor. The same cannot be said for the PdPt film, seen in 6.4 b) which means the increased resistance must result from different mechanisms which could not be elucidated.

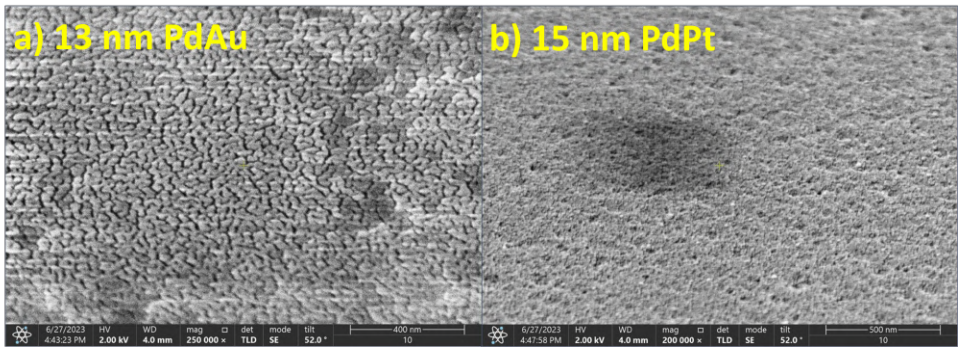

Fig. 6.4: a) PdAu, clear gaps between the islands explains the higher transmission. While in b) PdPt little to no island formation is observed which results in a lower transmission.

6.3 Transmission and electrical characterisation of gold

The last metal tested was pure gold (Au), which is widely utilised for transparent conductive coatings due to its high electrical conductivity. Furthermore, gold is known for its highly inert nature which in contrast to thin silver films does not corrode within minutes at atmospheric conditions [36]. Among all the metals examined, the Au films exhibited the most favourable transmission values, consistent with its dielectric function predictions. One striking feature of the gold films is the strong wavelength-dependent transmission, which due to its full d-orbital only undergoes interband absorption [53]. This means the prominent peak observed in figure 6.6 at approximately 500 nm can be explained using the same equation 6.1 for the bulk absorption modes that also predicts the transmission maximum for TiN at around 400 nm in figure 6.1. This wavelength-dependent behaviour is characteristic of the material and plays a significant role in its optical properties.

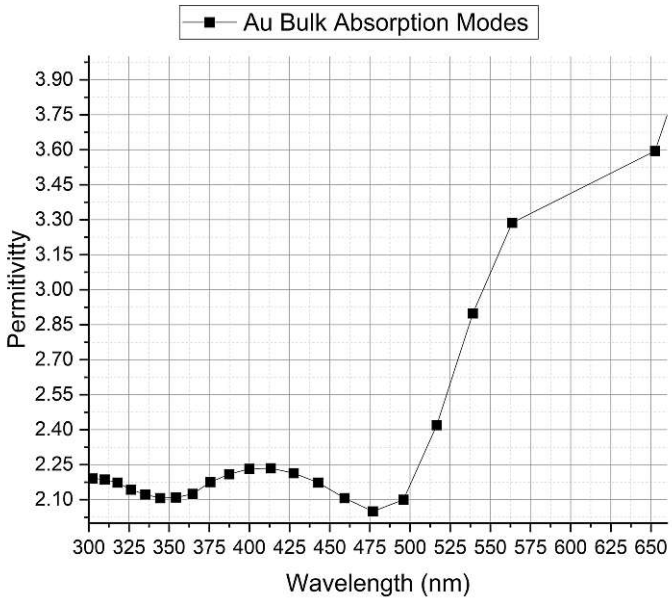

Fig. 6.5: Theoretical bulk absorption modes of Au, with the 500 nm maximum transmission peak clearly visible.

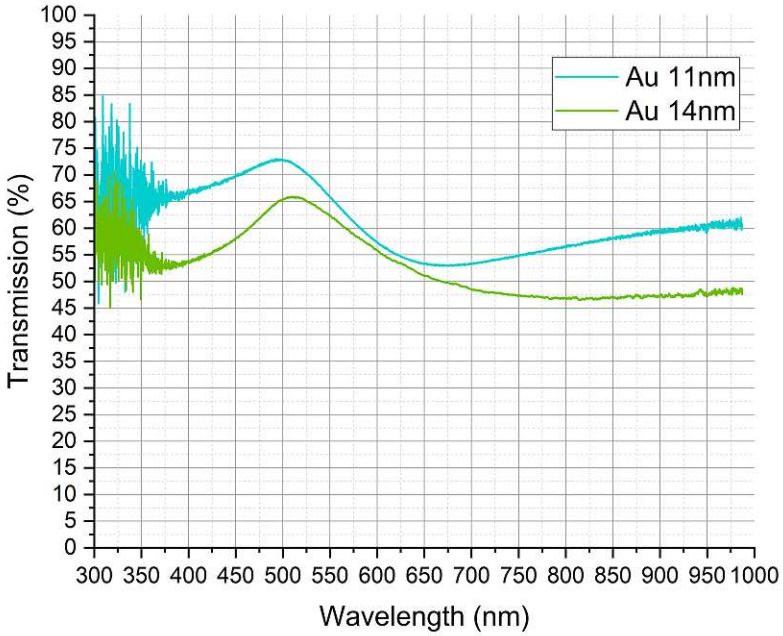

Fig. 6.6: A comparison of the transmission of the two gold films. In both films the transmission maximum can be seen that is theoretically predicted using the dispersion relation and material constants. In the thinner film the plasmon polariton induced transmission loss dip is clearly visible at 660 nm.

In the gold spectrum seen in figure 6.6, the presence of a distinct transmission minimum at around 660 nm is particularly evident in the 11 nm gold film. This phenomenon arises from the formation of isolated islands of gold that are not in electrical contact with each other, which is reflected in the sheet resistance in table 6.4. These electrically isolated islands undergo what is known as plasmon polariton interaction, resulting in selective absorption of specific wavelengths by the metal-dielectric surface structures. A surface plasmon polariton is an electromagnetic surface wave which is formed when an incident photon has the appropriate energy to interact with free outer shell electrons [60]. Since this process is sensitive to certain wavelengths only particular wavelengths are absorbed due to this interaction. The plasmon polariton interaction is more pronounced in thinner films where the islands are more widely separated. As the film thickness increases and the islands become more connected, the plasmon polariton interaction gradually diminishes which is also visible in figure 6.6 where the 14 nm film no longer displays a clear absorption minimum. Therefore, this transition from isolated islands to a connected network correlates not only with an increase in electrical conductivity but also a reduction of wavelength dependant absorption mechanisms [61]. These gold films vividly illustrate the effects of percolation and island formation, serving as a clear demonstration of the essential role that film homogeneity and connectivity play in determining their electrical and optical properties.

Tab. 6.4: The extent of the disconnected islands of Au films is reflected clearly in the sheet resistance of the films, where the isolated islands in the 11 nm are not able to conduct electricity.

Au thickness	Sheet resistance Ω/□
11 nm Au	Non-conductive
14 nm Au	24.6 ± 2.5

The formation of gold droplets on the surface of Borofloat substrates can be attributed to the stronger adhesive forces between the gold atoms compared to the gold-substrate interaction. As a consequence, driven by the desire to minimise free surface energy the gold atoms coalesce into droplets rather than spreading uniformly over the surface. This behaviour is evident in the SEM images displayed in figure 6.9, where spaces between the droplets indicate the lack of a homogeneous film [62].

6.4 Investigating gold thin film characteristics with Al_2O_3 wetting layers

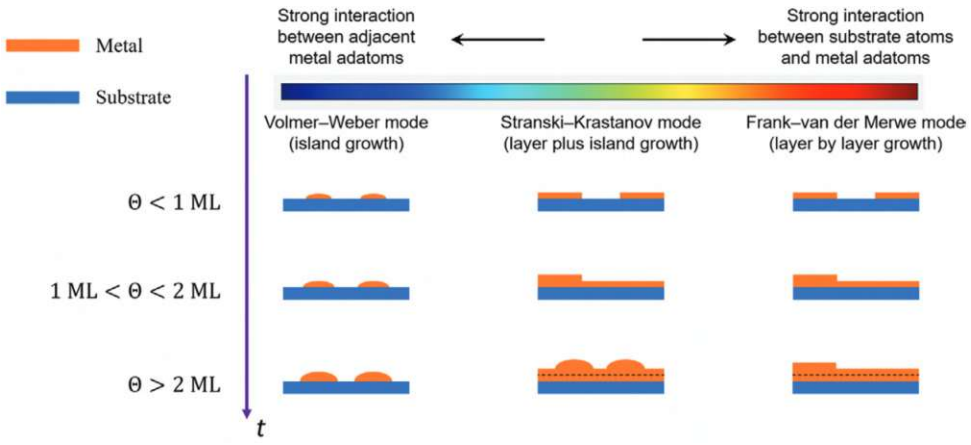

Fig. 6.7: An overview of the different growth mechanisms of thin films depending on the interaction strength of the growing film and the substrate. These growth modes can be classified using Youngs equations for the contact angle between two materials. The growth mechanism can also be tuned by the deposition temperature [36].

The growth of gold films on the Borofloat substrate follows Vollmer-Weber growth, as depicted in figure 6.7 above. Consequently, the resulting film exhibits a rough surface morphology and lacks consistent connectivity which is also visible in figure 6.9. This issue is not unique to this study but is a prevalent challenge in industry, leading to extensive investigations on how to minimise surface energy between the two materials and enable the formation of homogeneous films. One approach to address island growth is the introduction of wetting layers, typically dielectrics in the form of metal oxides. While the precise mechanism of wetting layers has not been fully elucidated, it is believed that the incorporation of metals in the oxide facilitates interfacial chemical reactions, thereby enhancing surface wettability and reducing free energy [36].

In our study, we opted to utilise aluminium oxide (Al_2O_3) as a wetting layer, deposited using Atomic Layer Deposition (ALD). The choice of Al_2O_3 was justified by its capability to be deposited at a low thickness, thereby reducing absorption losses, and its compatibility with CMOS fabrication processes. While other oxides like silicon oxide do not offer any wettability, the preference in iterature leans towards transition metal oxides [63].

Two thicknesses of Al_2O_3, namely 2 nm and 5 nm, were employed, followed by approximately 11 nm of gold deposited using thermal evaporation. An overview of the two films can be seen in figure 6.8. Despite a 10% deviation in the measurement of the thickness of the deposited gold film, as the wafers were coated in the same run, it was assumed that this is a local deviation, and the average thickness of both gold films over the entire wafer remains consistent.

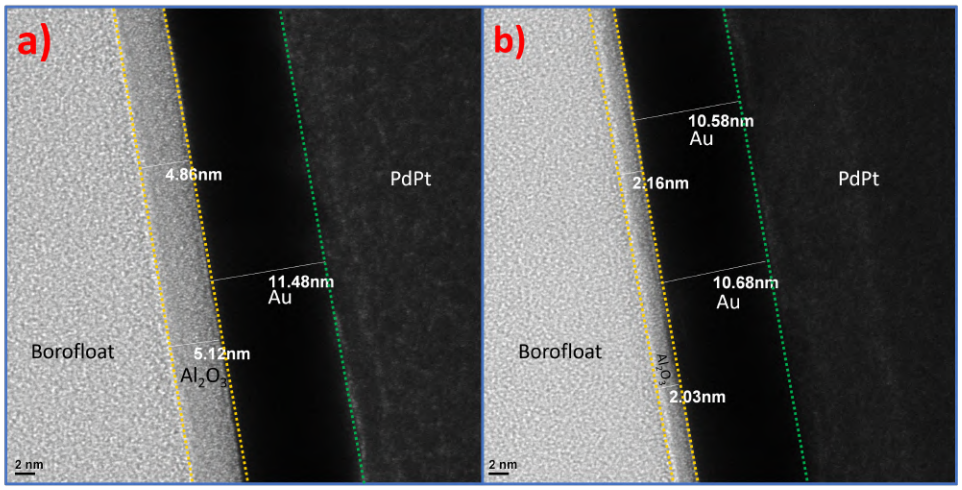

Fig. 6.8: Using TEM the exact structure and thickness of the gold films could be measured.

TEM imaging in figure 6.8 enabled a precise examination of the thickness and cross-sectional morphology of the deposited films. Upon close comparison of the surface of the gold films using SEM in figure 6.9, it becomes evident that the gold deposited on thicker 5 nm Al_2O_3 in panel d) exhibits fewer gaps between the islands compared to gold on the 2 nm Al_2O_3 in panel c). The impact of Al_2O_3 thickness on the film properties is illustrated in table 6.5, where the gold film on 5 nm Al_2O_3 shows half the sheet resistance compared to that deposited on 2 nm of Al_2O_3. This difference is likely due to the 2 nm film not yet fully assuming the bulk induced surface structure of Al_2O_3. Nevertheless, the 2 nm of Al_2O_3 serves a purpose, as the 11 nm gold film deposited on it exhibits similar resistivity to that of the thicker 14 nm film without Al_2O_3 (table 6.4. Which can be expected since the surface morphology seen in figure 6.9 b) and c) display similar island size and connectivity. Although this experiment successfully investigated the wetting layer abilities of Al_2O_3, a comprehensive characterisation of the transmission properties was not feasible due to contamination class restraints in the fabrication tool park.

Tab. 6.5: An overview of the influence of the thickness of the wetting layer on the sheet resistance

Material Stack	Sheet resistance Ω/□
11 nm Au + 5 nm Al_2O_3	11.3 ± 0.5
11 nm Au + 2 nm Al_2O_3	25.1 ± 1.8

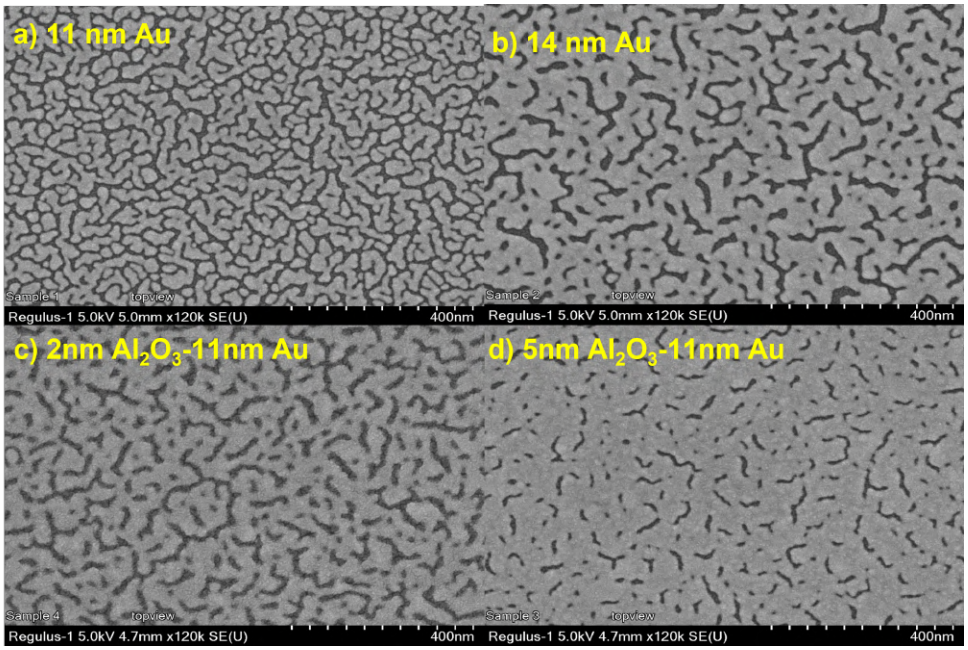

Fig. 6.9: An overview of the surface of all four gold films that were investigated. A clear trend towards smoother surfaces can be identified in the increase of the gold thickness improving the island connectivity and gap sizes. On top of this, a clear increase in film homogeneity can be seen when Al_2O_3 is used as a wetting layer.

6.5 Evaluating thin film metals potential as TCs

The selection of metals or metal alternatives, presents a wide range of possibilities and potential as transparent conductive coatings. However, TiN shows the least promise due to its low transmission values and conductivity. In cases where fabrication toolparks do not allow the use of gold, TiN could serve as an alternative, although its transmission and conductivity values are suboptimal. The best resistivity values were achieved by incorporating a wetting layer for gold deposition. Even before that, gold demonstrated the best transmission and resistivity values among all the tested metals. Furthermore, further optimisation of gold deposition and wetting layers could potentially improve these values even more, as already shown in existing literature [36].

However, the transmission values of all investigated metals fall short compared to what can be achieved using other materials, particularly the transition metal oxides mentioned earlier. Due to their superior transmission qualities they will therefore also be examined further in chapter 8. Additionally, the metals used in these investigations can only be deposited using physical vapor deposition methods, limiting their ability to adequately cover surfaces with high aspect ratios. Although this method works well for coating flat surfaces with precision, suitable for a grating coupler shown in figure 6.10 (see yellow coatings labeled “1”). However, since efforts have been made to incorporate optics that need coverage on both the top as well as the side walls (see blue coatings labeled “2” in figure 6.10), metallisation using gold becomes impossible for the sidewall dielectrics in these scenarios.

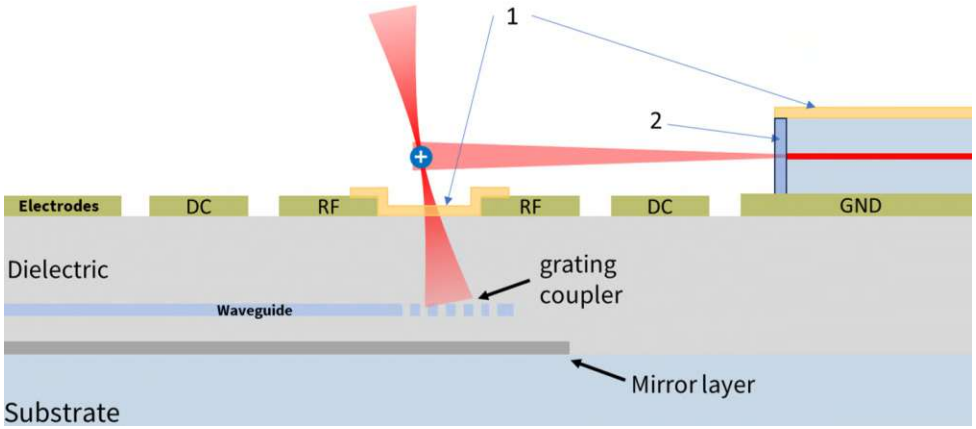

Fig. 6.10: This schematic shows the different optical integration techniques that have been considered in this thesis as well as the areas where dielectrics need to be covered with TCs. Areas denoted with "1" can be covered using line of site deposition and therefore accessible to metals. The area denoted with "2" can no longer be reached with these techniques and therefore requires a different deposition technique. The different methods are described further in 7, for area "1" physical vapour deposition can be used and for "2" chemical vapour deposition.

Chapter 7

Deposition techniques and their role in sidewall coverage

The standard processes for depositing metals can be classified into a method called physical vapor deposition (PVD). In this process, the substrate is transformed into a vapor state and then transported to the sample surface where it condenses. This transport can occur naturally through the energy in the particles or with the aid of an electric field, but the outcome remains the same. The recondensation from the gas phase back into the solid state happens in a directed path, which is in the line of sight from the vaporised substrate. Consequently, it becomes extremely challenging to coat holes or trenches with high aspect ratios using this method [64].

The second class of deposition techniques is known as chemical vapor deposition (CVD). In this process, precursors react or decompose on the surface to form the desired film. Unlike PVD, CVD is not primarily used for depositing metals; rather, it finds application for other covalent or ionic materials. Since the precursors are introduced into the reaction vessel in the gas phase, they can be controlled to uniformly cover the entire surface of a sample. Once on the sample surface, they can further react to form the desired film. The capability to cover the entire surface uniformly is of great significance when coating sidewalls or high aspect ratio structures, such as for the integrated photonics in this work [65].

By altering the angle of the sample and subsequently rotating it, attempts were made to achieve sidewall coverage using PVD processes. Below in figure 7.1 a,b) SEM images depict an endeavour where PVD was used for a sidewall coating. However, even when depositing very thick films, ensuring the connectivity between the top and side coatings could not be guaranteed. This poses a problem as the entire coating should be grounded to avoid the presence of a floating metal, which could be detrimental to the stability of ions. In comparison in panels c) and d), a sample that employed ALD for sidewall coating is shown which displays perfect coating of the sidewall as well as the top surface.

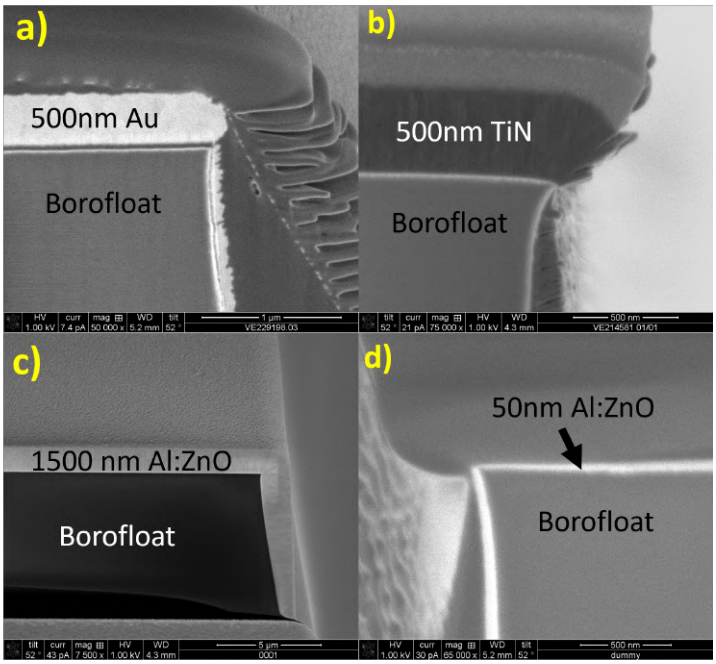

Fig. 7.1: These SEM cross-sections of the glass sidewalls offer a means to assess the sidewall coverage achieved by the deposited films. In the images denoted as a) and b), corresponding to the deposition of Au and TiN, respectively, some degree of sidewall coverage is observed. However, it was found that this coverage could not be achieved consistently in a reproducible manner. Moreover, there is a lack of electrical connection between the top layer and the sidewall metallisation in these cases. Conversely, the SEM images of the deposited AZO in c) and d) reveal remarkably uniform sidewall coverage, even at thin thicknesses of only 50 nm.

Chapter 8

Investigating Al:ZnO as a transparent conductive oxide

As mentioned in section 4.5, there is a class of materials that has been extensively developed by academia and industry for over a century. These materials encompass various metal oxides that have been doped to exhibit electrical conductivity while maintaining their optical transparency and have found widespread application in touch screens and photovoltaics [66]. Among the many doping types and metal oxides available, the main focus lies on Cu_2O, SnO_2, ZnO and In_2O_3. All of these oxides have demonstrated bulk resistivity values in the range of $10^{-4}\,\Omega/\square$ and consistent transmissions over 90% in the visible range [41]. Each of the four metal oxides mentioned above can be considered for different applications based on their unique material properties, such as coefficient of thermal expansion, thermal conductivity, hardness or chemical compatibility. However, In_2O_3 and ZnO have seen the highest incorporation into industrial processes due to them possessing the highest conductivity and transmission characteristics. Additionally, both oxides can be deposited using either CVD or PVD techniques.

In_2O_3 is typically doped with tin to form Sn:In_2O_3, commonly known as indium tin oxide (ITO). On the other hand, ZnO does not have a dominant dopant and is often doped with either Ga, Al, or F, with similar success for all dopants. In this research, Al:ZnO (AZO) was utilised, simply due to ease of precursor procurement. ITO is preferred in the industry as the go-to TCO due to its higher chemical inertness, which is crucial for applications like solar panels which are exposed to prolonged high temperatures [67] or biosensors susceptible to interaction with acids or bases [68]. However, for our application, operating at low temperatures and under UHV conditions, chemical stability is less relevant. Furthermore, indium is an expensive, rare and difficult to refine metal, since ITO often contains 90% indium, its manufacturing cost is significant. Additionally, ALD is a time and precursor-intensive process in general, making indium deposition using ALD even more expensive. In contrast, Al:ZnO uses the same precursors as Al_2O_3 and ZnO, both of which are already widely used in CMOS fabrication and therefore available at low prices, well controlled in terms of purity, and easily deposited [42].

ZnO is inherently an n-type semiconductor with an intrinsic conductivity ranging from 0.1 to $10^3\,\Omega{\cdot}$cm. Unlike silicon, the intrinsic conductivity in ZnO is not driven by thermally induced charge carriers, but rather by intrinsic defect donors such as oxygen vacancies or zinc interstitials. There have been suggestions that interstitial hydrogen may also naturally occur and act as a dopant. However, a more prevalent and effective dopant is aluminium, which substitutes zinc sites in the crystal lattice, enabling one electron, not involved in bonding, to transition into the conduction band. AZO also has a steep conduction band, facilitating high electron mobility [69].

8.1 Deposition of Al:ZnO

The AZO thin films used in this study were deposited using a hot walled ALD process, which involves cycles of diethyl zinc-H_2O and a cycle of trimethylaluminium-H_2O, the sum of these cycles is called a supercycle. The number of supercycles is repeated until the desired thickness is reached, for 1.5 µm AZO roughly 300 supercycles were needed. The specific ratio of zinc to aluminium in the deposition cycles resulted in a roughly 4% aluminium doping of the ZnO. This doping level should introduce approximately $10^{21}\,\mathrm{cm}^{-1}$ charge carriers. However, an excessive concentration of carriers can cause the plasma frequency to shift from the IR region to the visible spectrum, resulting in coloured films. Additionally, high doping levels may introduce more ionised impurities, leading to an increase in scattering sites and ultimately lowering the material's conductivity [43].

8.2 Transmission and electrical characterisation of thin film AZO

The initial AZO films, with thicknesses ranging from 40-50 nm, were deposited on both Borofloat substrates and tetraethyl orthosilicate (TEOS)-coated Si wafers. To ensure strong adhesion, a thin layer of Al_2O_3 was first deposited. The subsequent figure 8.1 provides an overview of the film thicknesses on the TEOS substrates. The distinct films are clearly distinguishable in the TEM image, and to verify the composition, an Energy-Dispersive X-ray Spectroscopy (EDS) spectrum was taken along the indicated arrow in figure 8.1. It is worth noting that the counts observed in the spectrum cannot be interpreted quantitatively due to a lack of a reference sample.

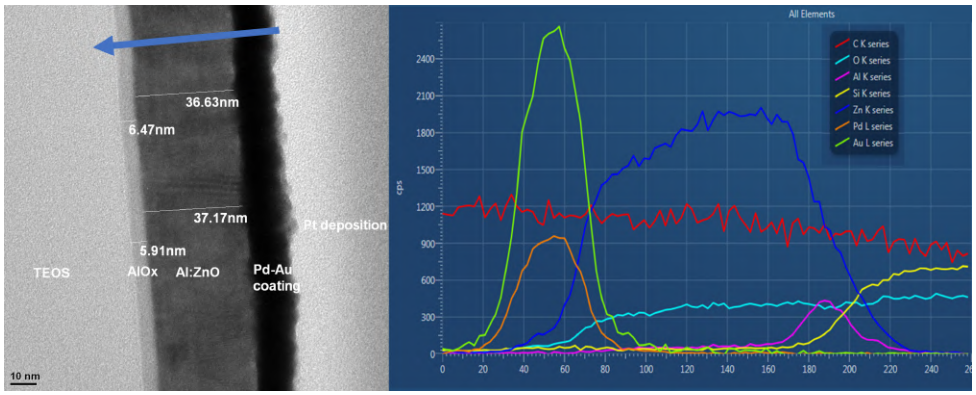

Fig. 8.1: A cross-section of a deposited AZO thin film was made using TEM. The films deposited using ALD are extremely homogeneous. On the right is an EDS spectrum of the same sample along the arrow, the x axis in nm does not reflect film thicknesses in the TEM image, this can be attributed to the lower resolution and larger spot size used in EDS.

Another film was deposited on a 500 µm Borofloat substrate to analyse its transmission characteristics. The corresponding spectrum is presented in figure 8.2. The film on the Borofloat substrate exhibited a slightly higher thickness, approximately 64 nm.

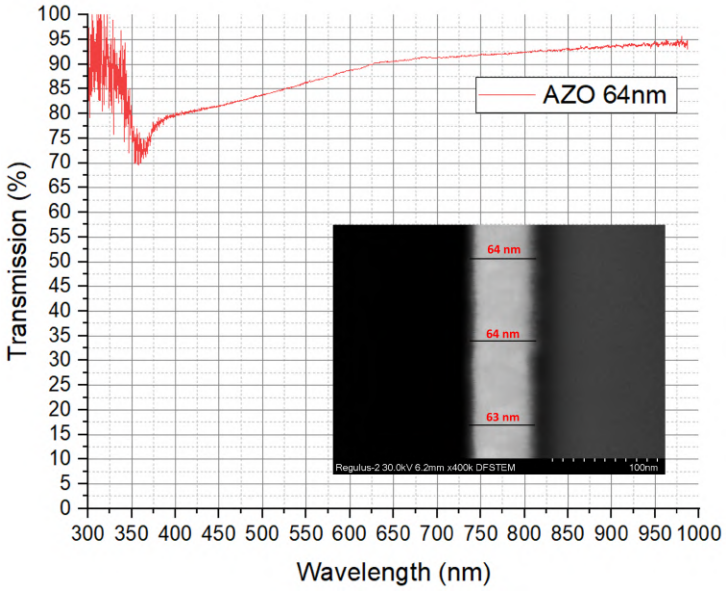

Fig. 8.2: Here the transmission spectrum of a 64 nm AZO thin film can be seen with the corresponding TEM image.

The measured spectrum in this work exhibits similar transmission characteristics to those reported in literature. Slight differences may arise from systematic errors in the constructed setup, as well as discrepancies in the film properties influenced by the deposition characteristics and methods. Nevertheless, the spectrum obtained in this study aligns with similar films, showing a higher transmission at longer wavelengths and a decrease in transmission towards the UV range. The resistivity values are also comparable, though most literature values are closer to the $10^{-4}\,\Omega$ boundary. This achievement should be easily reached through the optimisation of the deposition process [70]. An overview of the sheet resistance of the nm thick AZO films can be seen in table 8.2, notably these value are almost an order of magnitude higher than those measured for thin metal films examined in chapter 6.

An interesting feature that can be estimated from the transmission spectrum is the band gap, which is approximately 3.37 eV or 370 nm, it may vary slightly depending on the doping concentration and deposition methods. In the transmission spectrum, a distinct dip occurs at 370 nm, as the AZO starts to absorb photons due to photoexcitation. However, contrary to expectations, the transmission does not drop to 0% for shorter wavelengths. This observation can be attributed to two main factors. Firstly, the halogen bulb used produced very low photon counts in the region between 300-370 nm, which were further reduced when measuring the Borofloat as a baseline. Consequently, the counts were so low that when the Borofloat counts were set as 100% transmission, in fact, a value very close to the background noise was set as 100% transmission. Secondly, the film's extremely thin nature, following equation 4.3, did not absorb light perfectly, thereby enabling some transmission to occur.

Tab. 8.1: The sheet resistance values for thin film AZO.

AZO thickness	Sheet resistance $\Omega/\square$
37 nm AZO	690 ± 10.3
64 nm AZO	521 ± 20.7

8.3 Transmission and electrical characterisation of thick Film AZO

In addition to experimenting with thin AZO films, thicker films exceeding 1.5 µm were deposited on Borofloat substrates to assess potential improvements achieved by minimising surface scattering as a resistance contributor. On top of this, this film also allowed for the evaluation of the primary transmission loss mechanisms of the films. Concerns may arise about potential inhomogeneities in doping due to the formation of banded structures during the deposition process, involving Al_2O_3 and ZnO during supercycles [70]. However, upon examination of the EDS map of the TEM cross-section in figure 8.3, it becomes evident that there was a homogeneous distribution of aluminium throughout the ZnO. The small band of high Al concentration visible in the purple image in figure 8.3 can be attributed to the Al_2O_3 deposited before the AZO for adhesion purposes.

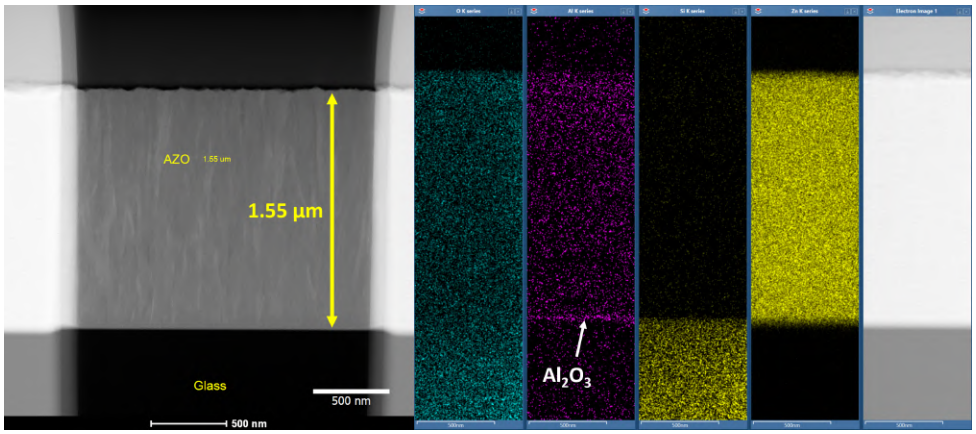

Fig. 8.3: Here a TEM cross-section of a thick AZO sample has been made in order to measure the precise film thickness. On the right hand side an EDS map of the same cross-section was made to deduce the elemental distribution of the film.

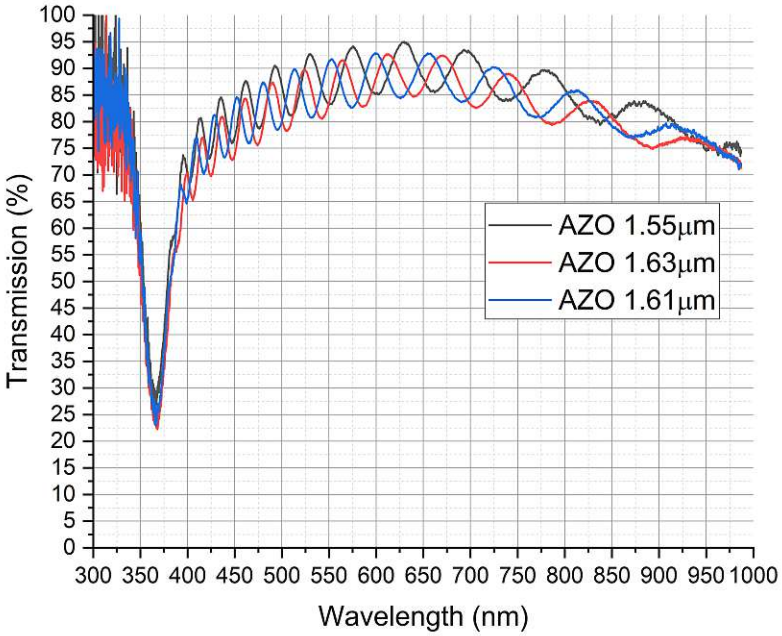

Fig. 8.4: Here the transmission spectra for various thicknesses of AZO is shown. The different thicknesses transmit roughly the same amount of light averaged over the entire spectrum but show higher transmissions at certain wavelengths.

As was the case for the nanometre thick AZO films the transmission characteristics of the thicker micrometre films were also examined. Due to constructive and destructive interference at specific wavelengths displayed in figure 8.4 caused by thin film interference, thicker AZO films exhibited higher wavelength dependant transmission than the 64 nm film in figure 8.2. The thicker AZO films also demonstrated much-improved sheet resistance values, nearly two orders of magnitude lower, as shown in table 8.2, in comparison to the thin films in table 8.1. The achieved conductivity and transmission characteristics aligned well with those reported in literature [71].

The resistivity values for the thick films can be assumed to be close to those found in a bulk structure due to the high film thickness used. The resistivity values measured $1.27{\cdot}10^{-3}\,\Omega{\cdot}$cm were also similar to those found in, literature $3{\cdot}10^{-3}\,\Omega{\cdot}$cm [72].

Tab. 8.2: The sheet resistance values for the three thickness of thicker AZO that were investigated. There is no real correlation between thickness and resistance which allows for the assumption that this is the bulk resistance of AZO and the variation can be attributed to different process parameters and natural measurement fluctuations.

AZO thickness	Sheet resistance Ω/□
1.55 µm AZO	8.20 ± 0.02
1.61 µm AZO	8.45 ± 0.25
1.63 µm AZO	8.33 ± 0.51

8.4 Investigating the growth and deposition characteristics of AZO

The growth mechanisms of AZO were also examined since these greatly influence a film's properties. Given the nature of the deposited films and the similarity in surface energy between metal oxides and the glass substrate, island formation was not expected. Additionally, since ALD deposition occurs layer by layer, Vollmer-Weber growth was not anticipated, but rather a Frank-der-Merwe growth. A closer look at SEM images in figure 8.5 provided further insights into the growth and crystal structure of the films. Notably, no distinct grain boundaries were observed, a finding that was confirmed in the TEM images in figure 8.3 and the Atomic Force Microscopy (AFM) images in figure 8.7. The densely packed dendritic or fibrous structures visible in the SEM images indicated that the film was in the Thornton transition zone between polycrystalline and amorphous [73].

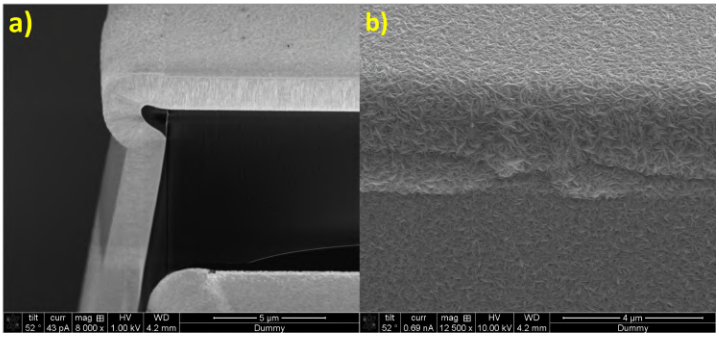

Fig. 8.5: a) is a SEM image of the cross-section of a 1.55 µm AZO film. Looking closely one can see the fibrous structure of the film perpendicular to the surface. b) the surface of the same film as in a) has been examined where early stages of columnar grain peak formation can be seen.

8.5 Further investigation of the properties and behaviour of AZO Films

8.5.1 Investigation into the transmission losses of AZO

The quantification of light energy transmitted through the thick and thin AZO films was achieved by integrating the area under their respective transmission curves seen in figure 8.6, as summarised in table 8.3. This provided the first indication of the main factors contributing to light loss during the transmission process. A more conclusive evaluation emerged inadvertently as a result of the ALD deposition process, where the samples were not securely fixed to the deposition chamber floor, coating the Borofloat wafer on both sides. To rectify this, a 11.7 M KOH etch was applied for five minutes on the reverse of the sample to remove the backside AZO coating. The impact of this backside AZO removal on the transmission values is depicted in figure 8.6 below. It should be noted that the samples used to gather the transmission data in previous chapters already had the second layer of AZO removed using this etch.

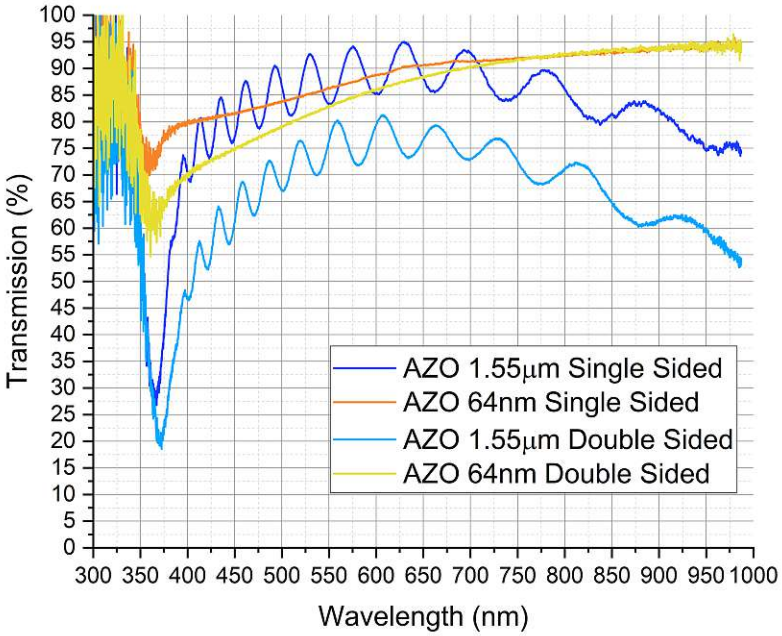

Fig. 8.6: Here the influence of two films on the transmission characteristics can be seen. From this graphic it is visible that the interface scattering and reflection are the highest loss contributors to the transmission of the films.

By comparing the integration values, it is clear that the reflection losses between the interfaces play the largest role in optical losses. Increasing the film thickness from 64 nm to 1550 nm incurs almost the same optical loss as when simply adding another 64 nm and interface. This observation suggests that reflection or scattering losses at an interface are more significant factors influencing the overall optical transmission than an increase in absorption due to film thickness.

Tab. 8.3: A quantification of the transmission of the AZO samples displayed in 8.6. The integral was performed over 370-950 nm as was the average transmittance.

AZO thickness	Integral Figure of Merit	Average Transmittance (%)
1.55 µm AZO Single Sided	4.844	83.45
1.55 µm AZO Double Sided	3.917	67.47
64 nm AZO Single Sided	5.216	89.91
64 nm AZO Double Sided	5.051	85.79

Additionally, this phenomenon of the constructive interference in these thicker films resulted in high wavelength-dependent transmission, which holds significant implications. Unlike solar panels that require high transmission across all wavelengths, ion traps only require specific wavelengths. Therefore, it is possible to deposit AZO films with tailored thicknesses that combine the advantageous wavelength specific transmission characteristics with the high bulk conductivity of thick films.

8.5.2 Kelvin Probe Force Microscopy (KPFM) analysis of AZO

As previously described, in ion traps, precise control over electric fields is crucial, as surface effects and potential fluctuations on surfaces may play a role in decreasing the quality of the potential well and increasing heating rates of an ion. To evaluate the role that an AZO surface could play in producing potential fluctuations, KPFM was used to investigate the surface potential landscape of a thick AZO film [74]. The figure 8.7 shows the result of $10\times10\,\mu m^2$ AFM and KPFM images that were taken simultaneously of the same surface area. The potential landscape is very uniform and shows few fluctuations. The lack of potential features can be attributed to two factors: first the lack of topological structure, and secondly, the AZO film does not have grain boundaries, which are known to accumulate charges through impurities [75].

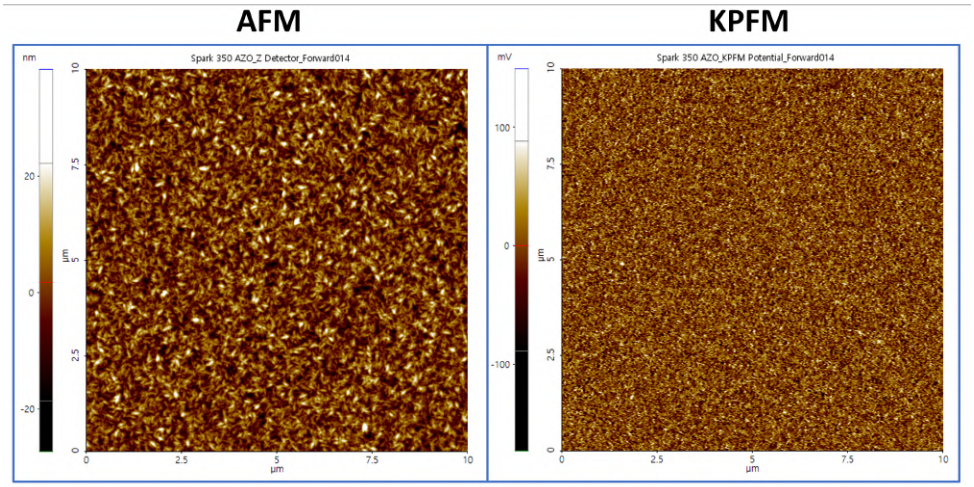

Fig. 8.7: A side by side comparison of the surface of an AZO film in AFM and KPFM. Although the image size is the same, the feature size in the potential landscape are much smaller than that in the topological map.

8.5.3 Annealing effects on AZO

As AZO films have been successfully characterised and identified as an optimal candidate to mitigate unwanted dielectric noise in an ion trap, the next crucial step is to incorporate this material into a CMOS compatible workflow. A thermal annealing process can significantly influence the properties of AZO. The polycrystalline as well as amorphous structure suggests that there is a possibility for potential improvements to the AZO film's characteristics which could be achieved through thermal annealing, which promotes grain growth, modifies charge carrier distribution and allows dopant activation. This phenomenon has also been reported in the existing literature with varying outcomes [76, 77]. On top of investigating potential improvements of the film, when designing a workflow, engineers must carefully consider the thermal budget. Processes involving substrate heating, for example metal deposition or plasma etching, can induce structural changes in the deposited materials as well as diffusion. For AZO, this could result in reduced conductivity, potentially due to the reduction of oxygen vacancies. To investigate the influence of annealing, two 37 nm AZO samples were subjected to a nitrogen atmosphere and underwent thermal treatment at 200 and 300°C with specific ramps, heating-cooling rates set at 5°C per minute, and a dwell time of 60 minutes.

While the expected processes for an AZO film involve short exposures to temperatures not exceeding 150°C for only a few minutes, we decided to evaluate worst-case scenarios. Table 8.4 records the resistivity values before and after the process. Interestingly, the AZO film exposed to 200°C showed minimal change in resistance, but the film exposed to 300°C exhibited a substantial increase in resistance. This higher temperature likely reduced the number of oxygen vacancies, leading to decreased conductivity. This observation is supported by the equation 8.2 below, which correlates the oxygen partial pressure to the number of free electrons in the film [69]. Furthermore, annealing AZO in a nitrogen atmosphere at 300°C could lead to nitride formations, which are non-conductive in the case of aluminium. Surprisingly, as observed in the AFM images in figure 8.8, there was no sign of grain nucleation even after annealing at 300°C. However, this could be attributed to the comparatively low temperatures used in our study compared to other literature works [78]. For a more definitive confirmation of crystalline AZO formation, x-ray diffraction would be a recommended analysis method. Therefore, in processing AZO to mitigate the loss in conductivity, it is essential to maintain low temperatures during processes since introducing reducing gases into standard procedures is not feasible.

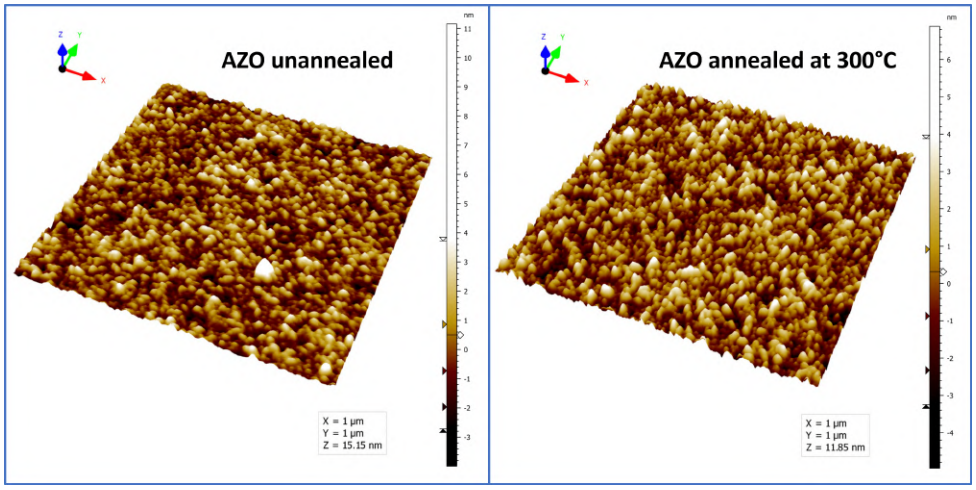

Fig. 8.8: This image indicates a slight change in the surface structure after the anneal, the unannealed AZO has an RMS of 1.193 nm and the annealed of 1.346 nm. This very small discrepancy could be attributed to the two different samples that were investigated as well as simply a local roughness deviation. However, AZO is known to have increased surface roughness after an annealing process [78].

$$M_2O_3 \Leftrightarrow 2M_{Zn} + 2e + O_O + 1/2O_2, \tag{8.1}$$

Which can be used to derive the oxygen partial pressure influence on electron concentration

$$[e] = [M_{Zn}] \sim p_{02}^{-1/8} \tag{8.2}$$

Where [e] is the electron concentration and p_{02} the partial pressure of oxygen.

Tab. 8.4: A comparison of the sheet resistance values before and after the annealing process. As well as a control to characterise any measurement drifts.

	Before annealing	After annealing
AZO	Resistivity Ω/□	Ω/□
Control	673 ± 10.52	669 ± 8.87
Sample 1-200°C	731 ± 2.26	990 ± 6.44
Sample 2-300°C	730 ± 2.37	2305 ± 20.83

8.5.4 AZO sheet resistance at cryogenic temperatures

After investigating the influence of high temperatures on AZO, it was equally important to examine its performance at cryogenic temperatures. While AZO films have been shown to be sufficiently conductive at room temperature, their intrinsic charge carrier density can undergo freeze-out, similar to normal semiconductors. However, due to AZO's degenerate doping and subsequent metal behaviour, the resistivity is expected to decrease at lower temperatures due to the minimisation of phonon scattering. Since AZO showed a decrease in resistance due to temperature reduction this leads to the conclusion that its degenerate doping results in metal like conduction characteristics. While measuring the resistance of ITO at cryogenic temperatures has already been documented in literature, there were no available literature values for AZO. Table 8.5 compares the conductivity values of a 37 nm film at room temperature and 14 K. The results clearly indicate a reduction in AZO resistance at lower temperatures. The roughly 10% decrease in resistance that the AZO film experiences is similar to that what is shown in literature for ITO [79].

Tab. 8.5: The comparison of the sheet resistance of the same AZO sample under different temperature conditions shows a marginal increase in conductivity due to phonon reduction.

AZO resistance at 298 K	AZO resistance at 14 K
731 ± 2.26 Ω/□	662 Ω/□

Chapter 9

Conclusion

Many sources describing TCOs or proposing improvements often evaluate them using a figure of merit (FOM). The FOM can vary widely, ranging from a simple ratio of transmittance at 550 nm to sheet resistance, as defined in 1972, to more complex functions that are based on the power generation in photovoltaics [80]. However, existing FOMs used in other industries may not be applicable to our specific use case. For instance, the simple FOM based on transmittance and sheet resistance has limitations, as it yields the highest FOM value at 37% transmittance [81]. Moreover, most FOMs used for solar applications consider the entire solar spectrum, while trapped ions only interact with select wavelengths. Given these considerations, considerable effort was invested in devising a metric that can quantitatively evaluate which TC is best suited for trapped ion quantum computing. However, it was concluded that providing an overview of the potential candidates along with their characteristics, advantages, and disadvantages should enable engineers designing ion traps to select a suitable TC for their specific use case.

Table 9.1 provides an overview of all the TCs developed in this study, including ITO for comparison, and a final example of a feasible feature TC, manufacturable using the available facilities. Notably, the thin AZO exhibits unparalleled transmission capabilities; however, it also demonstrates nearly an order of magnitude higher resistance than other thin films examined. The highest conductivities were achieved with the gold-wetting layer stack and the thick AZO film, with the latter possessing significantly superior optical transmission. Among the options, the TiN film emerges as the most straightforward and dependable choice, as it readily integrates into CMOS or MEMS stacks, and the percolation thickness can be attained without additional efforts. Finally, it is speculated that an AZO-gold-AZO sandwich stack, or a similar derivative, may vastly outperform both the gold and AZO thick films, combining the strengths of both materials while maintaining a thinner film than those tested in this study.

Currently, there is still ambiguity regarding the most suitable thin film for effectively mitigating stray fields and electric field noise from dielectrics and different applications may require a tailored solution. Nonetheless, the experimental results obtained provide promising insights, indicating that the frontrunner candidate, AZO, exhibits the potential to fulfil this role in the given environment. AZO's exceptional conductivity across all temperatures ensures the transport of implanted electrons or other formed charges. Moreover, its high transmission values suggest that a significant amount of laser energy can reach the ion, although proper quantification is necessary. Additionally, AZO displays metal-like conductivity characteristics, enabling successful shielding of charges from reaching the ion through Thomas-Fermi shielding.

Tab. 9.1: A comprehensive overview of the investigated films as well as potential competitors.

Material	Range of thickness	Ω/□	T% @ 397 nm	T% @ 729 nm	T% @ 854 nm	T% @ 866 nm	Advantages	Disadvantages
Gold	15-20 nm	24.6 (14 nm)	53.49	47.86	46.76	47.34	-Easy deposition	-low hardness -low transmission -unwelcome in CMOS
1) Al_2O_3 2) Gold	10-20 nm	11.3 (11 nm)	tbd	tbd	tbd	tbd	-easy deposition -high conductivity	-low hardness -expected low transmission -unwelcome in CMOS
TiN	10-20 nm	109.8 (13 nm)	56.0	46.75	41.53	41.27	-easy deposition -CMOS compatible	-low transmission -low conductivity
Noble alloys	15-20 nm	135 (15 nm)	52.48	51.91	51.73	51.36	-homogeneous transmission spectrum -potential improvement with wetting layers	-low transmission -low conductivity -unwelcome in CMOS processes
Al:ZnO	1500-2000 nm	8.2 (1550 nm)	72.83	84.59	80.67	82.67	-cheaper than ITO -good transmission -high conductivity	
Al:ZnO	30-60 nm	690 (37 nm)	79.90	91.66	92.82	93.32	-cheaper than ITO -high transmission	-low conductivity
Sn:In_2O_3	10-2000 nm	26.5 (230 nm)	>70 [82]	>85 [82]	>80 [82]	>80 [82]	-high transmission -high conductivity	-expensive -not sustainable
1) Al:ZnO 2) Gold 3) Al:ZnO	tbd [36]							

Chapter 10

Outlook

The convergence of physics and cutting-edge material engineering offers captivating new opportunities to manipulate electromagnetic radiation. Just as gratings are employed to direct light towards ions, metasurfaces, a form of surface manipulation, can enhance various aspects of the investigated TCs. By structuring the surface, metasurfaces can improve the transmission properties of deposited films, creating anti-reflective interfaces [83]. Additionally, metasurfaces can be designed for both active and passive focusing elements, enabling the integration of additional focusing elements or compensating for fabrication tolerances in integrated photonics [84]. Moreover, hyperbolic metamaterials could be tailored to achieve exceptionally high optical transmission along one axis while maintaining conductivity in the perpendicular axis [85].

However, before implementing novel materials and structures, it is essential to conduct fundamental experiments that can significantly improve the films, as suggested throughout this study. One such approach that was used unsuccessfully in this work is the utilisation of annealing. Under the correct circumstances however it has been demonstrated to greatly enhance the characteristics of deposited AZO films [78]. Furthermore, annealing can effectively reduce the required thickness of gold-dielectric stacks for percolation to occur. In addition to Al_2O_3, other transition metal oxides commonly used in CMOS fabrication, such as ZrO_2 or HfO, warrant investigation as potential wetting layers for thin gold films. This exploration can lead to valuable insights and possibly improved performance. A compelling approach involves combining a wetting dielectric or even TCOs, followed by a thin film metal, and finally another TCO, which yields an optimal combination of high conductivity and transmission. While this may initially seem counterintuitive, considering the reflection between films as the primary cause of transmission loss, the proposed structure possesses inherent antireflective properties that effectively mitigate these losses [86].

In addition to enhancing the investigated films, it is imperative to thoroughly characterise them to address the unique challenges associated with ion trapping. All resistance measurements were performed using DC power, while ion traps, as previously explained, operate at RF frequencies typically in the MHz range. Understanding the behaviour of TCOs at these frequencies is crucial to ensure that no unexpected phenomena result in stray electric fields or increased resistance, which could adversely impact ion trapping. Moreover, investigating the outgassing properties of TCOs is of significant importance. Cryogenic resistivity measurements were conducted in an ultra high vacuum environment, revealing increased partial pressures. To mitigate the potential impact of outgassed particles on ion interactions, it is essential to thoroughly explore and understand this phenomenon.

Finally, just as university education offers valuable knowledge and unveils insights into physical phenomena, so does benchtop lab testing unveil certain characteristics of material properties. Yet, it remains a mere prelude, offering only a glimpse into the multifaceted challenges that

unfurl in the real world of ion trap fabrication and quantum computing operations. The ultimate validation lies in the successful integration of this research into real-life processes and applications.

Chapter 11

Appendix

Tab. 11.1: An overview of possible transparent conductors and their dopants that may be considered in ion traps

Stoichiometric formula	Dopants
Au	
Ag	Al, Cr, Ni, Cu, Ti
Cu	
Pt	
Al	
Ta	
W	
Sn	
Ti	
Ni	
Mo	
V	
TiN	
SnO_2	Sb, F, As, Nb, Ta, Cl
In_2O_3	Sn, Ge, Mo, F, Ti, Zr, Mo, Hf, Nb, Ta, W, Te
ZnO	Al, Ga, B, In, Y, Sc, F, V, S, Ge, Ti, Zr, Hf
CdO	In, Sn
Ga_2O_3	
TiO_2	
NiO	
CdS	
LaO	
CuS	
C (in the form of graphene)	
An unexhaustive amount of ternary and multinary materials which are normally combinations of the ones named above	
Cd_2SnO_4	
Zn_2SnO_4	
$ZnSnO_3$	
$CdSnO_4$	
ZnSnO	
Zn_2SnO	
Cd_2SnO	
$InGaZnO_4$	
$CuAlO_2$	

This list was compiled using the following sources: [36], [69], [52], [35], [87]

Bibliography

(1) Q.ai, *Quantum Computing Is Coming, And It's Reinventing The Tech Industry: = https://www.forbes.com/sites/qai/2023/01/24/quantum-computing-is-coming-and-its-reinventing-the-tech-industry/?sh=47237c9d14de*, 24.01.2023 (Accessed on 08.07.2023).

(2) Ezratty, O., *Understanding Quantum Technologies*, 5th Edition, 2022.

(3) Grimm, R.; Weidemüller, M.; Ovchinnikov, Y. B. In *Advances In Atomic, Molecular, and Optical Physics*; Elsevier: 2000; Vol. 42, pp 95–170.

(4) Hughes, M. D.; Lekitsch, B.; Broersma, J. A.; Hensinger, W. K. *Contemporary Physics* **2011**, *52*, 505–529.

(5) Zachos, E., *How a Student Took a Photo of a Single Atom: https://www.nationalgeographic.com/science/article/trapped-atom-photograph-long-exposure-competition-spd*, 14.02.2018 (Accessed on 08.07.2023).

(6) Malinowski, M. Unitary and Dissipative Trapped-Ion Entanglement Using Integrated Optics, Ph.D. Thesis, ETH Zurich, 2021.

(7) Ospelkaus, C.; Warring, U.; Colombe, Y.; Brown, K. R.; Amini, J. M.; Leibfried, D.; Wineland, D. J. *Nature* **2011**, *476*, 181–184.

(8) Bruzewicz, C. D.; Chiaverini, J.; McConnell, R.; Sage, J. M. *Applied Physics Reviews* **2019**, *6*, 021314.

(9) Poulsen, G. Sideband Cooling of Atomic and Molecular Ions, Ph.D. Thesis, Aarhus: University of Aarhus, 2011.

(10) Kajita, M., *Ion Traps: A gentle introduction*; IOP Publishing: 2022.

(11) Kienzler, D. Quantum Harmonic Oscillator State Synthesis by Reservoir Engineering, Ph.D. Thesis, ETH Zurich, 2015.

(12) Auchter, S.; Axline, C.; Decaroli, C.; Valentini, M.; Purwin, L.; Oswald, R.; Matt, R.; Aschauer, E.; Colombe, Y.; Holz, P.; Monz, T.; Blatt, R.; Schindler, P.; Rössler, C.; Home, J. *Quantum Science and Technology* **2022**, *7*, 035015.

(13) Ballance, C. J., *High-Fidelity Quantum Logic in Ca+*; Springer Theses; Springer International Publishing: Cham, 2017.

(14) Leupold, F. M. Bang-bang Control of a Trapped-Ion Oscillator, Ph.D. Thesis, ETH Zurich, 2015.

(15) Nägerl, H. C.; Leibfried, D.; Rohde, H.; Thalhammer, G.; Eschner, J.; Schmidt-Kaler, F.; Blatt, R. *Physical Review A* **1999**, *60*, 145–148.

(16) Hogle, C. W.; Dominguez, D.; Dong, M.; Leenheer, A.; McGuinness, H. J.; Ruzic, B. P.; Eichenfield, M.; Stick, D. **2022**, arXiv:2210.14368 [quant-ph].

(17) Kielpinski, D.; Monroe, C.; Wineland, D. J. *Nature* **2002**, *417*, 709–711.

(18) Seidelin, S.; Chiaverini, J.; Reichle, R.; Bollinger, J.; Leibfried, D.; Britton, J.; Wesenberg, J.; Blakestad, R.; Epstein, R.; Hume, D.; Itano, W.; Jost, J.; Langer, C.; Ozeri, R.; Shiga, N.; Wineland, D. *Physical Review Letters* **2006**, *96*, 253003.

(19) Romaszko, Z. D.; Hong, S.; Siegele, M.; Puddy, R. K.; Lebrun-Gallagher, F. R.; Weidt, S.; Hensinger, W. K. *Nature Reviews Physics* **2020**, *2*, 285–299.

(20) Mehta, K.; Ricci-Vasquez, A.; Mordini, C.; Beck, G.; Malinowski, M.; Stadler, M.; Zhang, C.; Kienzler, D.; Home, J. In *Integrated Optics: Devices, Materials, and Technologies XXVII*, ed. by García-Blanco, S. M.; Cheben, P., SPIE: San Francisco, United States, 2023, p 33.

(21) Ivory, M.; Setzer, W. J.; Karl, N.; McGuinness, H.; DeRose, C.; Blain, M.; Stick, D.; Gehl, M.; Parazzoli, L. P. *Physical Review X* **2021**, *11*, 041033.

(22) Niffenegger, R. J.; Stuart, J.; Sorace-Agaskar, C.; Kharas, D.; Bramhavar, S.; Bruzewicz, C. D.; Loh, W.; Maxson, R. T.; McConnell, R.; Reens, D.; West, G. N.; Sage, J. M.; Chiaverini, J. *Nature* **2020**, *586*, 538–542.

(23) Mehta, K. K.; Zhang, C.; Malinowski, M.; Nguyen, T.-L.; Stadler, M.; Home, J. P. *Nature* **2020**, *586*, 533–537.

(24) Kumph, M.; Henkel, C.; Rabl, P.; Brownnutt, M.; Blatt, R. *New Journal of Physics* **2016**, *18*, 023020.

(25) Ong, F. R.; Schüppert, K.; Jobez, P.; Teller, M.; Ames, B.; Fioretto, D. A.; Friebe, K.; Lee, M.; Colombe, Y.; Blatt, R.; Northup, T. E. *New Journal of Physics* **2020**, *22*, 063018.

(26) Teller, M.; Fioretto, D. A.; Holz, P. C.; Schindler, P.; Messerer, V.; Schüppert, K.; Zou, Y.; Blatt, R.; Chiaverini, J.; Sage, J.; Northup, T. E. *Physical Review Letters* **2021**, *126*, 230505.

(27) Harlander, M.; Brownnutt, M.; Hänsel, W.; Blatt, R. *New Journal of Physics* **2010**, *12*, 093035.

(28) Zahn, M., *Electromagnetic field theory: a problem solving approach*; Wiley: New York, 1979.

(29) Ashcroft, N. W.; Mermin, N. D., *Solid state physics*; Holt, Rinehart and Winston: New York, 1976.

(30) Rogachev, A. Electrostatic screening in metals and electrolytes. (Thomas-Fermi and Debye approximation), University of Utah.

(31) Drude, P. *Annalen der Physik* **1900**, *306*, 566–613.

(32) Kittel, C., *Introduction to solid state physics*, 8th ed; Wiley: Hoboken, NJ, 2005.

(33) Maier, S. A., *Plasmonics: fundamentals and applications*; Springer: New York, 2007.

(34) Le Ru, E. C.; Etchegoin, P. G., *Principles of surface-enhanced Raman spectroscopy: and related plasmonic effects*, 1st ed, OCLC: ocn229031783; Elsevier: Amsterdam ; Boston, 2009.

(35) Gao, J.; Kempa, K.; Giersig, M.; Akinoglu, E. M.; Han, B.; Li, R. *Advances in Physics* **2016**, *65*, 553–617.

(36) Zhang, C.; Ji, C.; Park, Y.-B.; Guo, L. J. *Advanced Optical Materials* **2021**, *9*, 2001298.

(37) Smoliner, J., *Grundlagen der Halbleiterphysik: Was Studierende der Physik und Elektrotechnik wissen sollten*; Springer Berlin Heidelberg: Berlin, Heidelberg, 2020.

(38) Neamen, D. A., *Semiconductor physics and devices: basic principles*, 4th ed, OCLC: ocn681739179; McGraw-Hill: New York, NY, 2012.

(39) MKS, C., *MKS Instruments Handbook Semiconductor Devices and Process Technology*; 2nd Edition; MKS: 2012.

(40) Callister, W. D.; Rethwisch, D. G., *Materials science and engineering: an introduction*, 8th ed, OCLC: ocn401168960; John Wiley & Sons: Hoboken, NJ, 2010.

(41) Dixon, S. C.; Scanlon, D. O.; Carmalt, C. J.; Parkin, I. P. *Journal of Materials Chemistry C* **2016**, *4*, 6946–6961.

(42) David, S. Electronic structure studies of p-type semiconducting oxides, Ph.D. Thesis, Dublin: Trinity College Dublin, 2011.

(43) Li, X. D.; Chen, T. P.; Liu, Y.; Leong, K. C. *Optics Express* **2014**, *22*, 23086.

(44) Lin-Kwang, J.; Ramey, S.; Reynes, J.; Hillard, R.; Thieme, T. *Microelectronics Reliability* **2000**, *40*, 1497–1502.

(45) Schroder, D. K., *Semiconductor Material and Device Characterization*, 1st ed.; Wiley: 2005.

(46) Jochen, T. In *Proceeding of the 18th Edition of the Multimedia in Physics Teaching and Learning Conference*, European Physical Society: Madrid, 2014.

(47) Instruments, A. ASEQ Instruments-LR1 – compact spectrometer Datasheet Version 2.1.

(48) Janesick, J. R., *Scientific charge-coupled devices*; SPIE Press: Bellingham, Wash, 2001.

(49) PGO High-quality borosilicate glass from SCHOTT-Special Properties, English.

(50) Macleod, H. A., *Thin-film optical filters*, Fifth edition; Series in optics and optoelectronics; CRC Press, Taylor & Francis Group: Boca Raton, 2018.

(51) Birkholz, M.; Ehwald, K.-E.; Wolansky, D.; Costina, I.; Baristiran-Kaynak, C.; Fröhlich, M.; Beyer, H.; Kapp, A.; Lisdat, F. *Surface and Coatings Technology* **2010**, *204*, 2055–2059.

(52) Gordon, R. G. *MRS Bulletin* **2000**, *25*, 52–57.

(53) Palik, E. D.; Ghosh, G., *Handbook of optical constants of solids*; Academic Press: San Diego, 1998.

(54) Steinhögl, W.; Schindler, G.; Steinlesberger, G.; Engelhardt, M. *Physical Review B* **2002**, *66*, 075414.

(55) Borah, S. M.; Bailung, H.; Chutia, J. *Progress in Color, Colorants and Coatings* **2010**, *3*, DOI: 10.30509/pccc.2011.75767.

(56) Burke, M.; Blake, A.; Povey, I. M.; Schmidt, M.; Petkov, N.; Carolan, P.; Quinn, A. J. *Journal of Vacuum Science & Technology A: Vacuum, Surfaces, and Films* **2014**, *32*, 031506.

(57) Johnson, P. B.; Christy, R. W. *Physical Review B* **1972**, *6*, 4370–4379.

(58) Krylov, I.; Qi, Y.; Korchnoy, V.; Weinfeld, K.; Eizenberg, M.; Yalon, E. *Journal of Vacuum Science & Technology A* **2020**, *38*, 032403.

(59) Cutnell, J. D.; Johnson, K. W., *Physics*, 4th ed; Wiley: New York, 1998.

(60) Burstein, E.; Chen, W. P.; Chen, Y. J.; Hartstein, A. *Journal of Vacuum Science and Technology* **1974**, *11*, 1004–1019.

(61) Axelevitch, A.; Apter, B.; Golan, G. *Optics Express* **2013**, *21*, 4126.

(62) Sennett, R. S.; Scott, G. D. *Journal of the Optical Society of America* **1950**, *40*, 203.

(63) Naidich, Y.; Zhuravlev, V.; Gab, I.; Kostyuk, B.; Krasovskyy, V.; Adamovskyy, A.; Taranets, N. *Journal of the European Ceramic Society* **2008**, *28*, 717–728.

(64) *Handbook of thin-film deposition processes and techniques: principles, methods, equipment, and applications*, 2nd ed; Seshan, K., Ed.; Noyes Publications: Norwich, N.Y, 2002.

(65) *Atomic Layer Deposition for Semiconductors*; Hwang, C. S., Ed.; Springer US: Boston, MA, 2014.

(66) Lewis, B. G.; Paine, D. C. *MRS Bulletin* **2000**, *25*, 22–27.

(67) *Gallium oxide: technology, devices and applications*; Pearton, S. J., Ren, F., Mastro, M. A., Eds.; Metal oxides series, OCLC: on1032023402; Elsevier: Amsterdam, Netherlands, 2019.

(68) Aydın, E. B.; Sezgintürk, M. K. *TrAC Trends in Analytical Chemistry* **2017**, *97*, 309–315.

(69) *Handbook of Transparent Conductors*; Ginley, D. S., Ed.; Springer US: Boston, MA, 2011.

(70) Zhai, C.-H.; Zhang, R.-J.; Chen, X.; Zheng, Y.-X.; Wang, S.-Y.; Liu, J.; Dai, N.; Chen, L.-Y. *Nanoscale Research Letters* **2016**, *11*, 407.

(71) Badgujar, A. C.; Yadav, B. S.; Jha, G. K.; Dhage, S. R. *ACS Omega* **2022**, *7*, 14203–14210.

(72) Dasgupta, N. P.; Neubert, S.; Lee, W.; Trejo, O.; Lee, J.-R.; Prinz, F. B. *Chemistry of Materials* **2010**, *22*, 4769–4775.

(73) Thornton, J. A. In ed. by Jacobson, M. R., San Diego, CA, United States, 1988, p 95.

(74) Flasch, C. Kelvin probe force microscopy analysis of microfabricated ion traps, English, Ph.D. Thesis, Vienna: Technical University of Vienna, 2023.

(75) Kaiser, N. *Applied Optics* **2002**, *41*, 3053.

(76) Petrova, D.; Napoleonov, B.; Minh, C. N. H.; Marinova, V.; Lan, Y.-P.; Avramova, I.; Petrov, S.; Blagoev, B.; Videva, V.; Strijkova, V.; Kostadinov, I.; Lin, S.-H.; Dimitrov, D. *Nanomaterials* **2023**, *13*, 800.

(77) Panigrahi, J.; Vandana; Singh, R.; Rauthan, C. M. S.; Singh, P. K. *AIP Advances* **2017**, *7*, 035219.

(78) Tong, H.; Deng, Z.; Liu, Z.; Huang, C.; Huang, J.; Lan, H.; Wang, C.; Cao, Y. *Applied Surface Science* **2011**, *257*, 4906–4911.

(79) Wiesel, M.; Birkl, G.; Ebrahimi, M. S.; Martin, A.; Quint, W.; Stallkamp, N.; Vogel, M. *Review of Scientific Instruments* **2017**, *88*, 123101.

(80) Anand, A.; Islam, M. M.; Meitzner, R.; Schubert, U. S.; Hoppe, H. *Advanced Energy Materials* **2021**, *11*, 2100875.

(81) Haacke, G. *Journal of Applied Physics* **1976**, *47*, 4086–4089.

(82) Liu, T.; Zhang, X.; Zhang, J.; Wang, W.; Feng, L.; Wu, L.; Li, W.; Zeng, G.; Li, B. *International Journal of Photoenergy* **2013**, *2013*, 1–8.

(83) Zhang, B.; Hendrickson, J.; Nader, N.; Chen, H.-T.; Guo, J. *Applied Physics Letters* **2014**, *105*, 241113.

(84) Arbabi, E.; Arbabi, A.; Kamali, S. M.; Horie, Y.; Faraji-Dana, M.; Faraon, A. *Nature Communications* **2018**, *9*, 812.

(85) Smolyaninov, I. I.; Smolyaninova, V. N. *Solid-State Electronics* **2017**, *136*, 102–112.

(86) Xie, J.; Bi, Y.; Ye, M.; Rao, Z.; Shu, L.; Lin, P.; Zeng, X.; Ke, S. *Applied Physics Letters* **2019**, *114*, 081902.

(87) Axelevitch, A.; Gorenstein, B.; Golan, G. *Physics Procedia* **2012**, *32*, 1–13.